COMPOSITION AND RHEOLOGY OF OVERTHICKENED LAVA FLOW UNITS ON BANKS PENINSULA, NEW ZEALAND

Presented to the Department of Geology of Colorado College
In Partial Fulfillment of the Requirements for the Degree
Bachelor of Arts

Ryan Kroner

May 2016

Table of Contents

List of Figures

List of Tables

Acknowledgements

My sincere thanks to Jeff Noblett for advising me on and editing my thesis from its beginning to its end, to Steve Weaver for guiding me in creating pressed and fused discs for XRF and XRD analyses and for performing the analyses themselves, and to Mandy for all her help over the past four years. Thanks also go to Sam Hampton and Darren Gravely, my New Zealand research advisors, for their involvement in this project, both in presenting the initial research concept to me and for providing crucial assistance at various stages in the process of the research. Thanks goes to the Frontiers Abroad geology program as a whole for providing the opportunity to study in New Zealand, as well as Megan Anderson for bringing the program to my attention. Thanks also goes to Nigel Hampton for providing crucial boat access, to Stephen Brown for XRF data and work, and to Rob Spiers for creating the thin sections used in the research. My thanks to all the CC faculty not already mentioned and to all the senior geology majors for making this such a fantastic department. I definitely chose the right major. Finally, I'd like to thank my family for their unwavering love and support.

Abstract

Exceptional coastal exposures of Miocene lava sequences on Banks Peninsula, New Zealand provide an opportunity to understand the emplacement processes of over-thickened lava flows. Field observations of three geochemically variable (nephelinite, hawaiite, and mugearite) over-thickened flows reveal 2-4 m-thick lavas inland that transition into ~50 m cliff-forming compound units toward the ocean. These cliff sections are the result of rapid emplacement of multiple flows that enable cooling as a single unit. Possible eruption rates and reconstruction of various emplacement mechanisms can determine controls on the over-thickening of the aforementioned lava examples.

Flow compositions modeled against temperatures and viscosities indicate that viscosities and compositions did not exert a significant influence on the over-thickened morphologies. There is no correlation between geochemistry (especially wt. %SiO_2) and the morphology of the overthickened flows, and the close relationship of viscosity to geochemistry suggests that viscosity is not a major factor in the emplacement of these overthickened flows. Computational analysis of viscosities, coupled with measurements of flow dimensions and crystal content, reveal that high effusion rates may have been a critical factor in forming these overthickened flows, with rates of between 400 and 2000 $m^3\ s^{-1}$ being likely. Production of more precise ranges of possible rates is hindered by uncertainties associated with taking dimensional measurements of flows as old, weathered, and poorly exposed as these. Additionally, a particularly large margin of error for flow temperatures prevents the drawing of any reasonably precise conclusions with regard to effusion rates. This example illustrates the problems inherent in attempting to quantify such precise numerical parameters for ancient lava flow units. It is very likely that paleo-topography was a very influential factor on these flows' unique morphologies. Further work should focus on significantly narrowing the margins of error for flow dimensions (thickness and width) and flow temperatures.

Chapter 1 – Introduction

Banks Peninsula, on the South Island of New Zealand, is the heavily eroded remnant of two mid-Miocene shield volcanoes, both products of intraplate volcanism. Outcrops in this region reveal a repeating sequence of 2-4 m-thick largely basaltic lava flow units punctuated by ash and lahar horizons and cut into by irregular scoria cone features. On the larger and younger of the two shield volcano remnants – the Akaroa Volcanic Complex – a few lava flows showcase distinct geochemical and morphological characteristics. One such unit, denoted SB-N, is the dominant feature of a small bay on the northeastern section of Banks Peninsula called Stony Bay. This unit significantly thickens to around 40-50 m toward the ocean, ending in a series of sheer sea cliffs that seem to comprise a single lava flow. Analogous morphologies appear at Northwest Bay (NWB-H) and East Okains Bay (EOB-M) nearby. Previous work showed that the Stony Bay overthickened flow unit had a low-silica nephelinitic geochemistry, which is unique among flows sampled from Banks Peninsula (Eeg & Hampton, 2014).

The aim of this study is to determine the cause of these odd morphologies through a series of qualitative and quantitative analyses of different geochemical and rheological parameters, searching for a common factor among the three flows that might explain their massive thicknesses. Three such quantitative parameters are the focus of this study. The first is geochemistry, which, especially with regard to silica content, is very closely tied to the second parameter, viscosity. Viscosities are analyzed using a quantitative model developed by Giordano et al. (2008). The final quantitative variable, effusion rate, is studied using a model (Tallarico et al., 2006)

which combines viscosity, temperature, and a series of physical flow dimensions to calculate effusion rates. Emphasis is placed on viscosity and effusion rate, in particular, because of the significant influence these two rheological parameters have on the emplacement and, thus, the morphology of a lava flow. This study hypothesizes that the excessive thickness of some sections of these flows might be related to abnormally high effusion rates, and constraining that parameter was thus the end goal of this research. An additional, more qualitative, variable – topography at the time of the flows' emplacements – is also analyzed for its influence on these overthickened morphologies.

Aside from untangling the specific case of these overthickened flow units, this research also serves as a case study on the feasibility of applying such precise numerical methods to flows as old, eroded, and poorly exposed as these. Many of the models used for these calculations were based on observations of active modern lava flows, and their effectiveness with respect to quantifying ancient flows is a focus. Areas of particular concern here are uncertainties associated with the flows' dimensions due to their poor exposures, along with certain parameters like flow temperatures and volatile contents, both of which were very difficult to accurately constrain with the time and resources on hand.

Chapter 2 – Geological Setting

Geology of New Zealand

Known largely for its abundant seismic and volcanic activity, New Zealand is one of the more geologically unique – and geologically active – regions in the world. Straddling the boundary between the Pacific Plate to its southeast and the Australian Plate to its northwest, it is the largest subaerial section of a continental fragment called Zealandia. This fragment, then joined with the Australian continent, separated from the supercontinent Gondwana in the late Cretaceous (approximately 95-90 Ma). By around 50 Ma, New Zealand had been completely separated from Australia via extensional tectonics. From 50 Ma to 25 Ma the tectonic regime switched to compressional processes (Campbell et al., 2012).

The NE-SW-trending Pacific-Australian plate boundary lies on the eastern side of New Zealand's North Island, which is a part of the Australia Plate. On the South Island, this plate boundary is best approximated by the active Hope Fault, south of which the South Island lies on the western edge of the Pacific Plate. This plate is currently subducting beneath the Australian Plate from east to west at a rate of 4-6 cm/year, explaining the ubiquitous volcanism on the North Island (mostly in a region called the Taupo Volcanic Zone). In comparison, the part of the South Island that comprises part of the Pacific Plate is much less volcanically active. The regime in this region is largely collisional, resulting in the formation of such features as the towering Southern Alps (Campbell et al., 2012).

Geology of Banks Peninsula

Standing in stark contrast to the widespread and diverse volcanism of the North Island of New Zealand are the comparatively sparse and unimodal volcanic centers of South Island. The most significant of these centers is the Banks Peninsula region, located near Christchurch on the southeastern coast of South Island, in the Canterbury province (**Figure 1**). This volcanic complex – and its sister system on the Otago Peninsula to the north – comprises a peninsula of extremely hilly terrain that stands in sharp relief to the topography of adjacent regions. It formed as an island directly off the coast of the Canterbury region, subsequently linking to the mainland of South Island by an accumulation of alluvial gravels sourced from the mainland (Sewell, 1988).

Banks Peninsula is dominated by the heavily eroded remnants of two composite shield volcanoes of Miocene age, both the result of intraplate volcanism. The older of these – the Lyttelton volcanic complex – formed between 11.0 and 8.7 Ma, and has a diameter of ~25 km^2, while the younger – the Akaroa volcanic complex – was active from 9.3 to 8.0 Ma, and has a diameter of ~35 km^2 (Hampton & Cole, 2009; Timm et al., 2009; Stipp & McDougall, 1968). The older Lyttelton volcanics rest on top of Permian-Triassic sediments and on late Cretaceous, intermediate to silicic volcanic rocks of the Mount Somers Volcanic Group (Timm et al., 2009).

A few smaller eruptive episodes occurred during and after these primary episodes, including the Mount Herbert volcanic group from 9.7 to 8.0 Ma, the Church-type lavas from 8.1 to 7.3 Ma, and the Diamond Harbour volcanic group

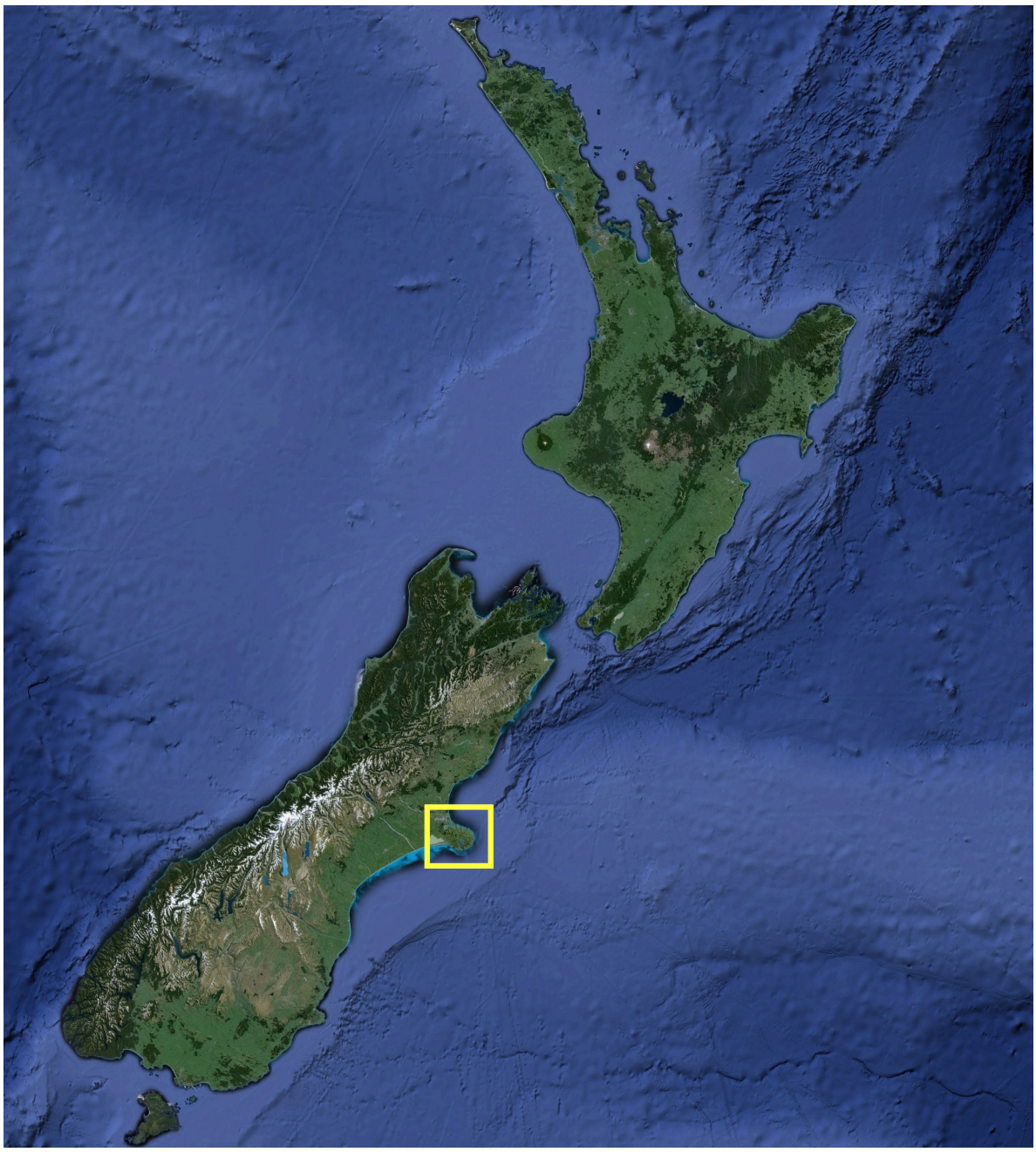

Figure 1 – The location of Banks Peninsula (denoted by a yellow box) relative to New Zealand as a whole. Imagery taken from Google Earth.

between 7.0 and 5.8 Ma (Hampton & Cole, 2009; Stipp & McDougall, 1968). The total volume for the entire volcanic complex is, at minimum, ~1750 km^3, with ~1200 km^3 for the Akaroa volcano, ~350 km^3 for the Lyttelton volcano, and 200 km^3 for the Mount Herbert and Diamond Harbour volcanic groups (Timm et al., 2009).

The landforms and volcanic deposits of the various eruptive phases of Banks Peninsula are dominated by sequences of moderately to highly mafic, low-silica lava flows stacked one on top of the other (Hampton & Cole, 2009). These lava flow sequences tend to be somewhat predictable both in their morphologies and their geochemistries, and are frequently separated by reddish ash, pyroclastic, lahar, or soil horizons. The flows serve to construct the primary volcanic cones, and can be linked to their primary vent or a number of secondary vents and parasitic cones. Thicknesses of the flows generally increase with proximity to the flow's vent, although paleo-topographic controls may play a role in the formation of different morphologies. Thicknesses for individual lava flow units are typically on the order of 1/3 m to 4 m, although this can vary significantly, with certain overthickened sections of some flows reaching tens of meters in thickness.

Other prolific volcanic landforms that can be found around the Banks Peninsula region include a number of scoria cones and associated volcaniclastic deposits. These generally occur along the outer flanks of their associated volcanic cones, and often cut through the lava flow sequences (Hampton & Cole, 2009). Also present throughout Banks Peninsula are features such as hypabyssal dikes and sills, as well as pyroclastic deposits, ash horizons, and a number of secondary erosional features.

The lava flows themselves generally fall along an alkalic basalt compositional trend, with the older Lyttelton volcanic complex consisting primarily of hawaiite flows (Price & Taylor, 1980). The younger Akaroa volcanic complex also contains a number of hawaiite flows but, relative to the Lyttelton lavas, displays lava compositions ranging from low-silica picrite basalts to hawaiite to mugearite to intermediate trachyte and benmoreite geochemistries and, in at least one case, nephelinite (Eeg & Hampton, 2014). The Lyttelton main phase lavas tend to display higher TiO_2, lower Na_2O/K_2O, and higher $MgO/(MgO + FeO^*)$ values compared to analogous Akaroa lavas (Price & Taylor, 1980). Flow textures range from aphanitic to mildly porphyritic to heavily porphyritic for both volcanic complexes, with averages falling toward the aphanitic end of the textural spectrum (Price & Taylor, 1980).

Research Approach

A multi-step analysis evaluates the factors that most influence the uniquely thick morphologies of the three lava flow units involved in this study. All the quantitative steps culminate in the modeling of the flows' viscosities and effusion rates as described in Chapter 3. Before these models were run, it was necessary to analyze the flows' compositions, evaluate petrography and flow textures, and determine their metric dimensions. The latter also led to some important qualitative analysis involving the role paleo-topography played in influencing their unique morphologies. This hierarchy of methodologies is outlined in the flow chart below (**Figure 2**).

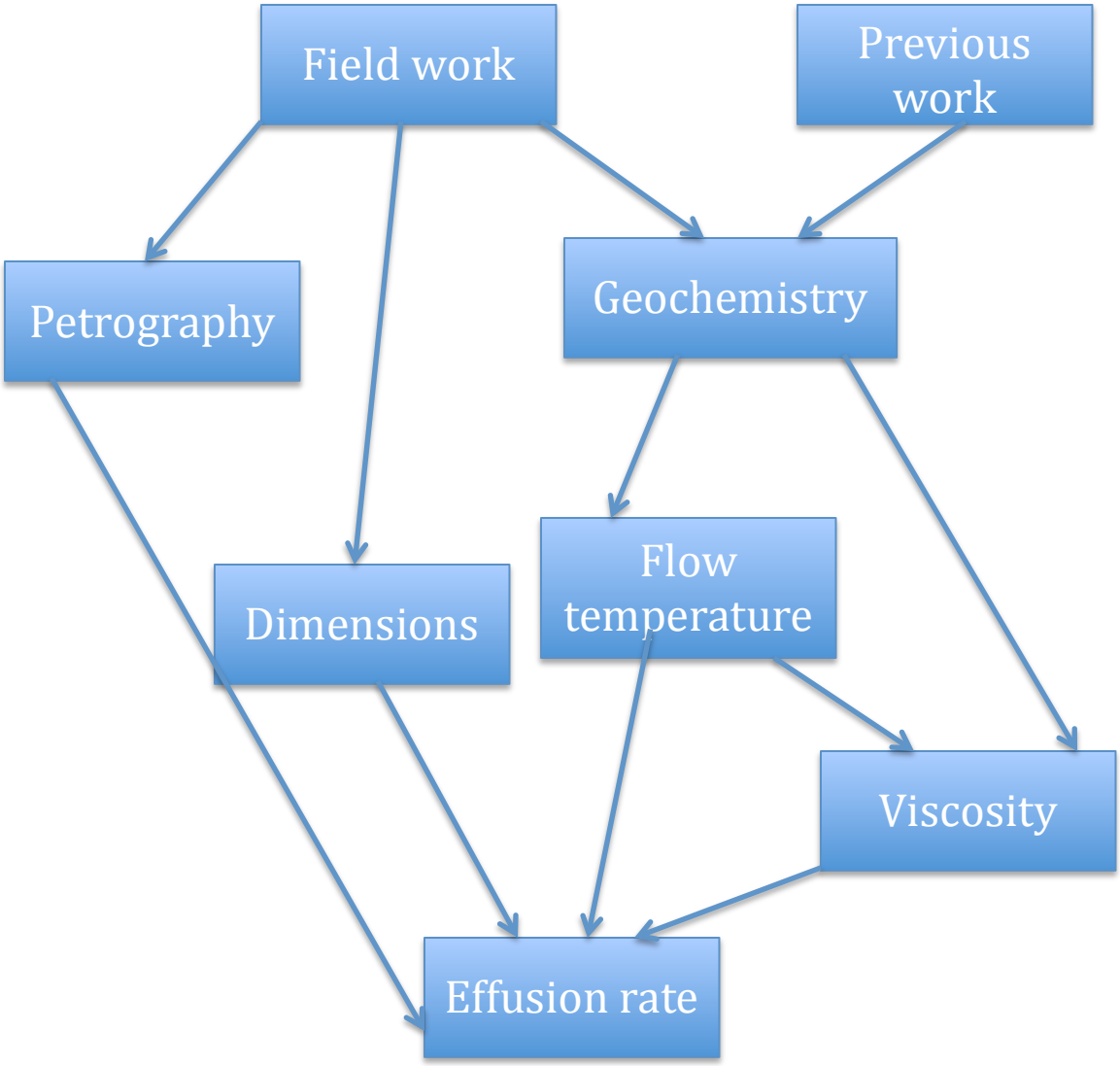

Figure 2 – Flow chart for the various steps taken in this research.

Chapter 3 – Modeling Approaches

Modeling Lava Flow Viscosity

Giordano et al. (2008) provides a comprehensive model that calculates the viscosity of a silicate melt as a function of melt temperature based on a set of major and minor oxide concentrations (SiO_2, Al_2O_3, TiO_2, FeO_2, CaO, MgO, MnO, Na_2O, K_2O, P_2O_5, H_2O, and F_2O_{-1}). This model, whose constituent mathematical components are briefly described below, is used to plot temperature against log[viscosity] for each sample in Microsoft Excel. The authors of the Giordano et al. (2008) paper very helpfully provide an Excel spreadsheet set up to run the model calculations automatically with an input of a set of oxide concentrations and a set range of melt temperatures.

The temperature range was initially based on estimates from the literature for the eruption temperatures of various lava types. However, subsequent work with the MELTS geothermobarometry program (Gualda & Ghiorso, 2015) was undertaken in an effort to better constrain the precision of temperature estimates, thus increasing the precision of all subsequent calculations that incorporated these temperature values. MELTS works by prompting an input of a set of major oxide concentrations along with a set range of temperatures over which values would be calculated. It then calculates a liquidus temperature for the composition at the given pressure value (Gualda & Ghiorso, 2015).

Central to the viscosity model is the Vogel-Fulcher-Tammann (VFT) equation (**Eq. 1**), in which *T(K)* is the temperature in Kelvins; *A* is a constant; *B* and *C* are

adjustable parameters, both dependent on oxide concentrations and molar weights of the oxides; and η is the viscosity, measured in Pa s (Giordano et al., 2008).

EQUATION 1 $$\log\eta = A + \frac{B}{T(K) - C}$$

A potential source of error in this process was due to the fact that, in the process of preparing the hand samples to be crushed and powdered for geochemical analysis, they were all left overnight in an oven in order to remove any volatiles that might interfere with the accuracy of the geochemical analysis. The viscosity model includes terms for volatiles H_2O and F_2O_{-1} in its calculation since a higher volatile concentration will have a noticeable effect on the viscosity of the melt (Giordano et al., 2008). However, due to the limitations of our analytical methods for geochemistry, all volatiles were necessarily eliminated, and the calculated viscosities are all anhydrous. Therefore, if the sampled lavas had a significant concentration of volatiles when erupted, melt viscosity would be underestimated.

Modeling Lava Flow Effusion Rates

Along with flow viscosity and temperature, the effusion rate of a lava flow exerts significant control on various aspects of that flow, including flow length and area covered, whether it is emplaced as a pahoehoe or an a'a lava flow, and the formation and size of lava tubes (Tallarico et al., 2006). The role of effusion rate in determining a flow's length is especially important, as this can be used to calculate

the potential hazards associated with a modern, active lava flow, and might be used to trace an ancient lava flow back to its source vent.

Similar to the process of calculating lava viscosities outlined above, modeling of effusion rates was based on mathematical models published by previous researchers. While much work has been done with effusion rates in the past, these papers largely focused on constructing models on data from active lava flows (Harris & Rowland, 2009; Patrick et al., 2004; Dragoni et al., 1995). Consequently, these models tend to employ variables that cannot easily be deduced from ancient lava flow units such as those on Banks Peninsula. However, Tallarico et al. (2006) developed a feasible model for determining effusion rates that depends on variables that can be determined, within reasonable levels of uncertainty, for the lava flow units at Stony Bay, Northwest Bay, and East Okains Bay. Certain variables in this model would be more precisely measured in an active lava flow, so calculations will still be somewhat less precise than for an ancient flow, but these uncertainties cannot be avoided with any model.

A brief overview of the model's primary components is given below. The model includes four different equations for determining effusion rates. The correct equation to use for a given flow is dependent on the ratios between certain physical properties of that flow (Tallarico et al., 2006). The first of these distinctions is that between the Bingham dynamics-based models and the Newtonian dynamics-based models. Newtonian rheologies are used to describe flows that are closer to the vent, where higher temperatures limit the exhibition of plastic behavior and deformation within the flow. Bingham rheologies, on the other hand, are used to approximate

flows that are farther from the vent, and are consequently cooler, therefore exhibiting dominantly plastic deformation. Tallarico et al. (2006) conclude that, to limit the uncertainty in the calculated effusion rates to 10%, the Bingham model should be used when the ratio of the plug thickness to the flow thickness exceeds 0.07. The flow thickness was measured in meters in the field. The plug height, however – also measured in meters – is a somewhat more abstract and less easily measured quantity that relates to the yield strength of the fluid in question.

Also called the 'critical depth' of a flow, the plug height is a quantity crucial to Bingham fluid dynamics and plastic flow behavior: if the flow thickness H is less than the plug height h_p, there will be no downhill movement of the flow. Plug height h_p is given by the equation (**Eq. 2**) below (Hulme, 1974; Tallarico et al., 2006). Variables in the following equations, with units and values, are defined in **Table 1**.

EQUATION 2

$$h_p = \frac{\tau_c}{\rho * g * \sin\alpha}$$

τ_c, the yield strength of the flow, is given by the following equation (**Eq. 3**), as per Harris & Rowland (2001).

EQUATION 3

$$\tau_c = 6500\emptyset^{2.85} + 0.01e^{0.08(T_e - T_c) - 1}$$

$\emptyset$, the total mass fraction of crystals within the melt, was approximated by examining the thin sections made from the lava flow units. T_e and T_c, the eruption and flow core temperatures, respectively, had to be inferred from known values, given that we lacked a means by which we could determine exact temperatures for

Variable	Definition	Value	Units
a	Flow width	variable	m
α	Slope angle	0.20	rad
g	Gravitational acceleration	9.81	m s^{-2}
H	Flow thickness	variable	m
h_p	Plug height	Eq. 2	m
$\emptyset$	Total crystal mass fraction	0.10-0.30	dimensionless
q_{3DN}	Effusion rate (3-D, Newtonian)	Eq. 4	m^3 s^{-1}
q_{3DB}	Effusion rate (3-D, Bingham)	Eq. 5	m^3 s^{-1}
τ_c	Yield strength	Eq. 3	Pa
T_e	Eruption temperature	1473	K
T_c	Flow core temperature	1400	K
μ	Flow viscosity	variable	Pa s

Table 1 – Variables in effusion rate models (Tallarico et al., 2006; Hulme, 1974; Harris & Rowland, 2001)

the flows in question. The slope angle, α, was approximated to 12.5° based on known slope averages around Banks Peninsula.

The next distinction among the four models developed by Tallarico et al. (2006) is that between two- and three-dimensional flow models. This depends on the ratio between the width and thickness of the lava flow in question. If this ratio (width/thickness) does not exceed 13, then the 3-D model must be used. If this ratio is over 13, then the 2-D model should be used. Since the flows observed in this study tended to have significant lateral extents, even in their thicker sections, the 2-D model was better suited to my calculations. Between Bingham and Newtonian rheologies, the lava flows in this study are more likely to have behaved with Bingham rheology unless their viscosities were unprecedentedly low. Thus, the equation used for most calculations was the two-dimensional Bingham model.

The 2-D Bingham (q_{2DB}) and Newtonian (q_{2DN}) models are described below, while the 3-D models can be found in Tallarico et al. (2006), and are not relevant to this study.

EQUATION 4a

$$q_{2DN} = \frac{\rho g \sin\alpha}{3\eta} a H^3$$

EQUATION 4b

$$q_{2DB} = \frac{\rho g \sin\alpha}{3\eta} a H^3 \left(1 - \frac{3}{2}\frac{h_p}{H} + \frac{1}{2}\frac{{h_p}^3}{H^3}\right)$$

Obtaining moderately accurate values for dimensional parameters, especially for flow thickness H and flow width a, was one of the primary goals of the fieldwork

described in Chapter 4. It is also an area of significant uncertainty due largely to the inconsistent and often poor exposure of the overthickened lava flows and due to the significant erosion that has taken place since they were emplaced. The models for effusion rate were run using the Wolfram Mathematica program, and the same program was used to create a series of plots for the model results.

Chapter 4 – Field Observations & Petrography

Field Methods

Time spent at the three field sites was dedicated to taking a number of samples from the overthickened flow units and recording qualitative observations, along with photographs of the outcrops in question. Samples were taken from the overthickened units at Stony Bay, Northwest Bay, and East Okains Bay. Due to time and accessibility constraints, only one sample was taken from the East Okains Bay flow unit. Sampling along all three units was also limited by the fact that they occur in outcrop as sheer sea cliffs: as such, it was difficult to obtain samples from more than the few accessible areas on each flow.

Due to its unique geochemical composition, its accessibility, and its relatively good exposure in most places compared to the other two primary lava flow units, the bulk of the field time available was allotted to working in Stony Bay and on flow unit SB-N. Using GPS measurements, careful constraints on flow contacts, widths, and thicknesses were acquired, with the rest of these dimensional quantities being estimated via satellite imaging. At Stony Bay, samples were also taken from flows immediately beneath SB-N and from flows on the other side of the bay; the latter in an effort to further constrain the width of lava flow unit SB-N (**Figure 3**).

In total, one sample was collected from EO-M, two from NWB-H, and twelve from SB-N. The latter two were supplemented by samples from previous field excursions that took one sample from Northwest Bay and four from Stony Bay, bringing those totals up to, respectively, three and sixteen samples.

Figure 3 – A panoramic view of the overthickened Stony Bay unit SB-N, with sampling locations (for the nephelinites) marked and labeled.

Field Observations & Significance

The three field sites (**Figure 4)**, are characterized by, among other unique qualities, their anomalously thick morphologies. Each is defined by a single morphologically dominant lava flow unit, all of which are part of the younger Akaroa volcanic complex, and are bounded above and below by red soil, ash, or lahar horizons and brecciated flow contacts (Eeg & Hampton, 2014). Their most distinguishing feature is the sheer thickness they display at their most seaward extent, reaching up to 60 m in vertical relief within a single exposure. This stands in stark contrast to the majority of lava flows throughout Banks Peninsula, especially given that there is no indication of a proximal source vent for any of the three flows, which can sometimes account for thicker-than-normal flow morphologies (Hampton & Cole, 2009). Travelling inland – for these field sites, roughly to the southwest – one can observe the flows rapidly and dramatically thinning back to dimensions much more typical of average Banks Peninsula lava flow units (approximately 3 to 5 m) over a distance of a few hundred meters.

Another unique feature ascribed to the primary flow units at each of the three field sites is an abundance of columnar joints and their stratigraphic relationship to potential boundaries within the larger flows. Intermittent series of discrete subhorizontal contacts are found throughout the massive flows and may represent individual flow horizons. These potential flow horizons are often bisected by subvertical columnar joints of low to intermediate degrees of maturity. This observation is of note due to the relationship of columnar joints to an emplaced

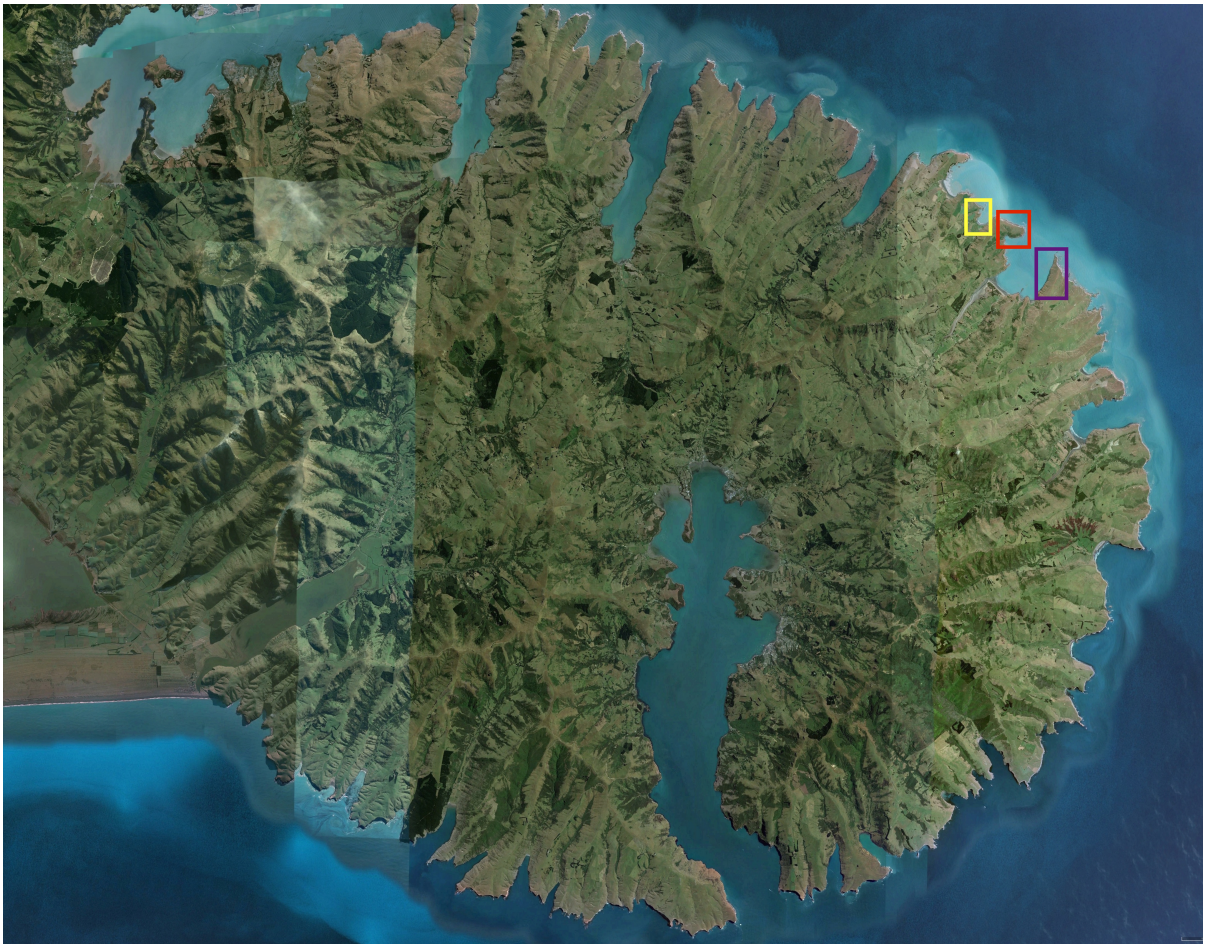

Figure 4 – The location of Stony Bay (yellow box), Northwest Bay (red box), and East Okains Bay (purple box) relative to Banks Peninsula as a whole. Imagery taken from Google Earth.

flow's thermal gradient, and because it may indicate that the section cooled as a single temporal unit.

The primary overthickened Stony Bay lava flow unit (termed SB-NP) achieves a maximum thickness of approximately 40-50 m, thinning landward to a more constant thickness of around 3-4 m, although this unit gets buried by soil and colluvium as it is traced in this direction (**Figure 5a**). This, along with increasingly heavy vegetation cover to the west/northwest and apparently significant degrees of erosion since emplacement, makes it somewhat difficult to accurately constrain its length and width (and its thickness, to a lesser extent). This exposure problem arises with all three flow units studied, and accounts for significant uncertainty in dimensional estimates. Directly beneath this flow unit is a reddish lahar deposit, which is then underlain by a breccia horizon and then the first of a sequence of moderately thick, much less morphologically unique lava flow units.

The primary overthickened lava flow unit at East Okains Bay – dubbed EO-M – is somewhat less prominent than that in the other areas, attaining a maximum thickness of roughly 20-25 m (**Figure 5b**). It also has greater lateral extent, making precise dimensional measurements somewhat difficult to obtain. Similarly, its columnar joints are irregular, immature, and poorly exposed compared to the NWB-H and SB-N units. Additionally, it slopes gently outward rather than rapidly thickening over the course of about 10 m like the Stony Bay and Northwest Bay flow units do. It is also the most eroded and poorly exposed of the three units, which, when combined with its significant lack of accessibility by anything other than boat, makes it a much more difficult flow to study than the other two. Therefore, aside

Figure 5a – Overthickened Stony Bay lava flow unit SB-N

Figure 5b – Overthickened East Okains Bay lava flow unit EOB-M

from geochemical studies, this study places less focus on the East Okains Bay flow than it does on the Northwest Bay and Stony Bay flows.

The thickest and most extensive of the three lava flow units is the Northwest Bay unit – referred to as NWB-H – which reaches a maximum of ~60 m in thickness toward the ocean. It is also somewhat wider and more extensive than the Stony Bay unit, and has a broad sea-facing cliff face that extends for hundreds of meters in either direction, lending itself to the best head-on exposures of the three field areas, allowing for observations taken from a boat. The columnar joints of unit NWB-H are somewhat more mature than those of SB-N, at times even beginning to display evidence of the polygonal faces and structures characteristic of archetypical, fully matured columnar joints. The unit is underlain by a reddish lahar layer. **Figure 6a** shows a photograph of the unit, while **Figure 6b** is a trace sketch highlighting the key features of the outcrop as exemplars for these features at all three overthickened units.

Aside from the sheer thickness of the flows in question, which reaches over 50 m for units SB-N and NWB-H, their most striking feature is the rapid change in thickness that characterizes the boundary of their massive sections. Sketched and annotated in **Figures 6a & 6b** for Northwest Bay [found in Chapter 4], this morphological transition presents a strong case for some amount of topographic control during the flows' emplacement in which the lavas may have flowed into a valley and run up against a wall. What we seek to accomplish throughout the rest of this study is to determine how much influence this factor had relative to other, more quantitative factors like viscosity and effusion rate during lava flow emplacement.

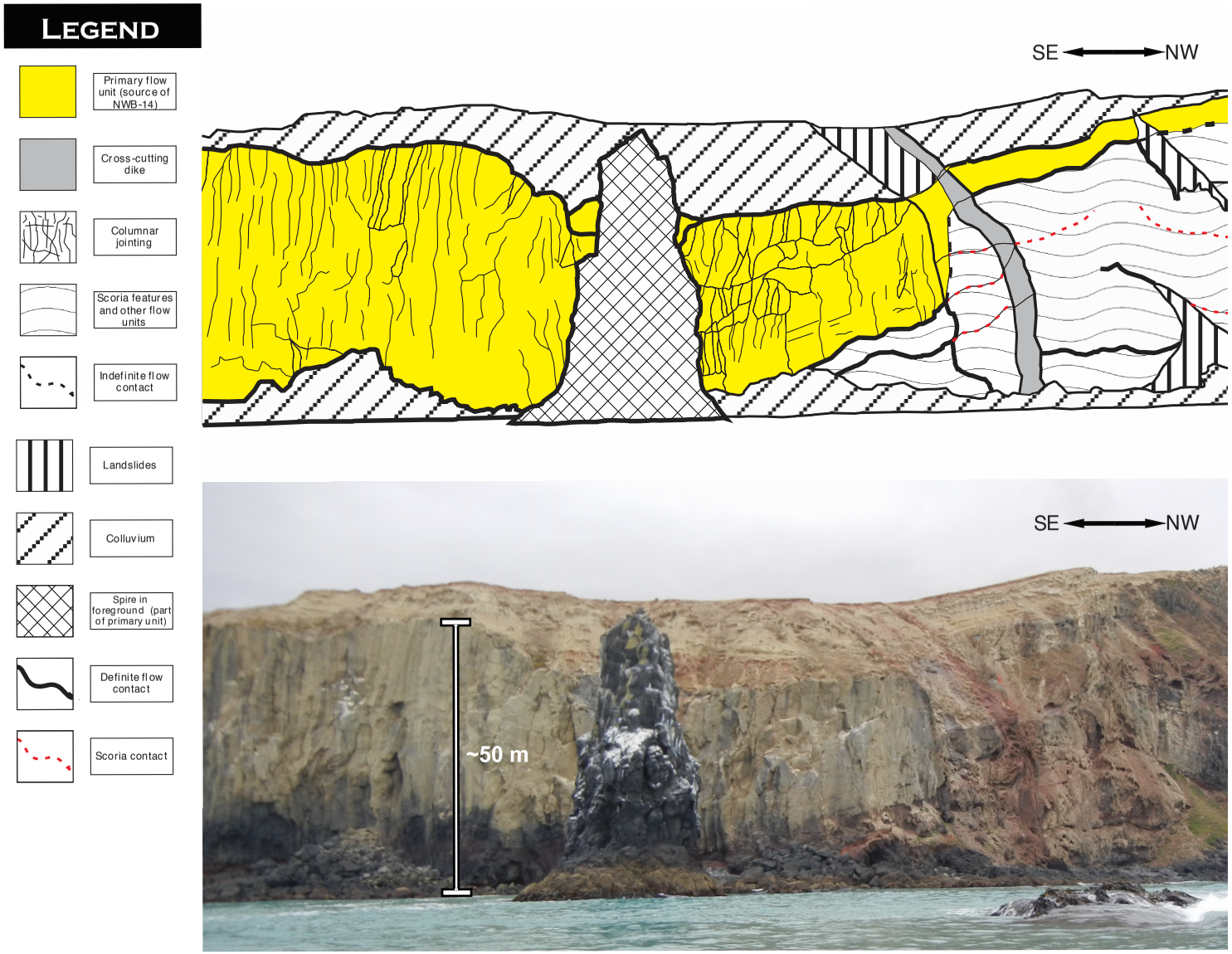

Figures 6a & 6b – A sketch of the features of interest in the overthickened sections of Northwest Bay flow unit NWB-H (above) and the photo upon which the sketch was based (below), with legend for the feature sketch on the left.

Petrographic methods

Polished thin sections were created for the six samples collected in my first field outing and analyzed at the UC (University of Canterbury) lab (four from SB-N, one from NWB-H, and one from EOB-M). Standard covered thin sections were made at Texas Petrology Labs for the twelve new Stony Bay samples and the two new Northwest Bay samples, all of which were collected in a second field outing a few months after the first. All thin sections were analyzed for significant petrographic features, focusing on finding and measuring potential flow textures within the overthickened flow units. Some of the NWB-H and SB-N samples were oriented in the field, thus allowing for measurement of any flow texture orientations that may exist.

Petrographic Observations & Significance

Due to the previously described difficulties in surveying and sampling lava flow unit EOB-M, it is excluded from that flow from the petrographic analysis. Thus, the primary focus is on the six samples taken from the overthickened nephelinitic Stony Bay lava flow unit SB-N (whose locations and sample IDs are shown in **Figure 3**). All six SB-N samples (SB2, 3, 4, 5, 7, and 10) have an aphanitic to slightly porphyritic texture consisting of a fine-grained crystalline groundmass interspersed with small to medium-sized phenocrysts. The latter population is dominated by olivine phenocrysts with occasional plagioclase feldspars and rare clinopyroxene crystals. Samples range from 4% to 10% phenocryst proportions, and also include

moderate amounts of opaque oxides that are usually more prevalent in the more weathered SB-N samples.

Flow textures are occasionally present in Stony Bay nephelinite thin sections. The best examples are found in sample SB3 and, somewhat less convincingly, SB5. SB3, in particular, contains elongated plagioclase and pyroxene groundmass crystals displaying parallel orientations suggesting flow and growth around the larger olivine phenocrysts in that sample (**Figure 7a**).

The two samples taken from the overthickened hawaiite unit at Northwest Bay, NWB-H, contain somewhat more porphyritic textures than the SB-N thin sections do. Phenocrysts comprise approximately 35% of the sections, and, like those from the SB-N samples, are dominated by olivine and plagioclase crystals. Olivine phenocrysts are more common, while plagioclase phenocrysts grow to much larger sizes. Flow textures in both samples and thin sections are similar to those observed in sample SB3, albeit more pronounced and with large plagioclase crystals orienting themselves around even larger phenocrysts (**Figure 7b**).

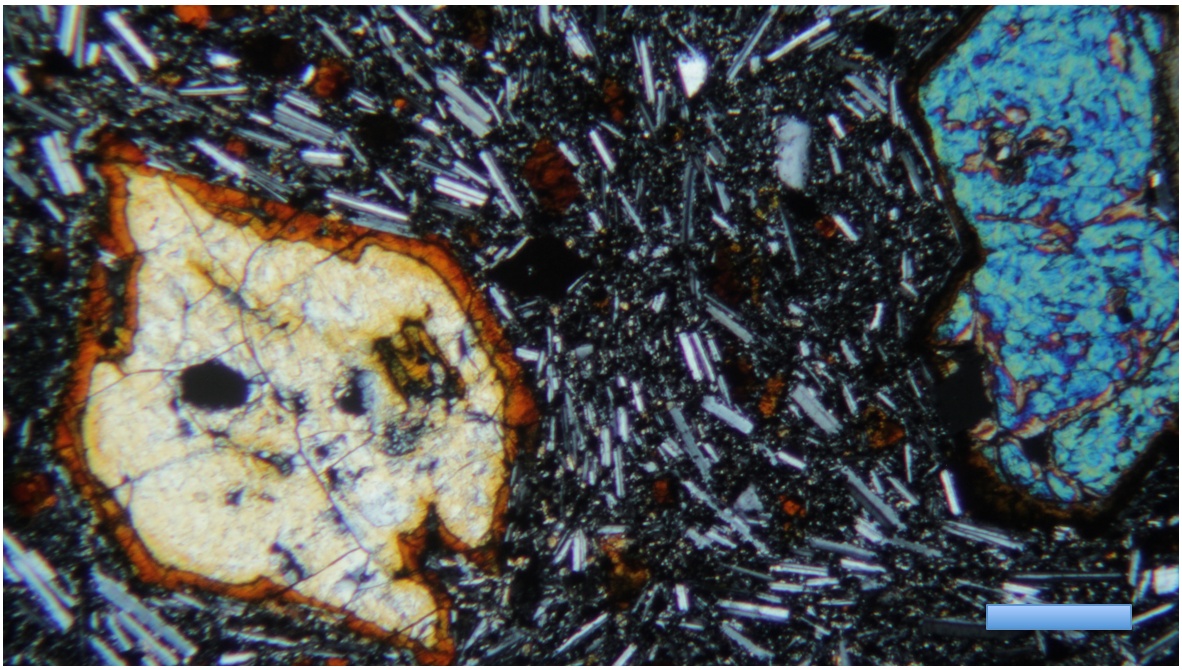

Figure 7a – 10x magnification view of the thin section created from sample NWB1, taken from flow unit NWB-H. The scale bar is approximately 0.2 mm.

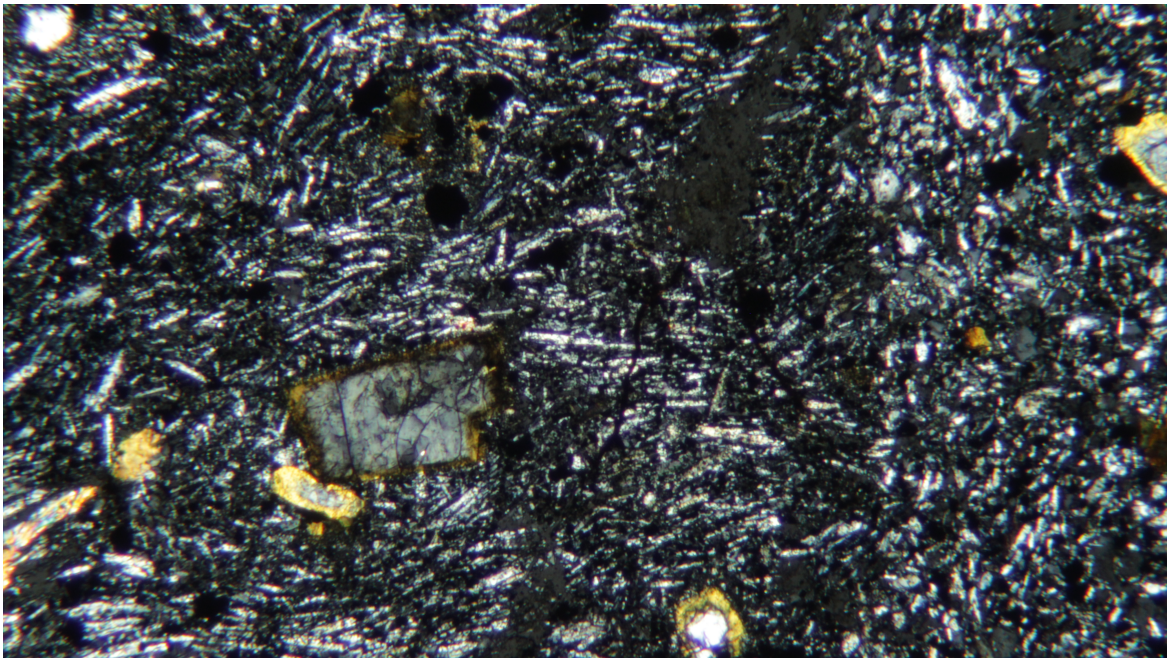

Figure 7b – 10x magnification view of the thin section created from sample SB3, taken from flow unit SB-N. The scale bar is approximately 0.2 mm.

Chapter 5 – Geochemistry

Geochemical Methods

Geochemistries of the twelve new Stony Bay samples and the two new Northwest Bay samples were analyzed using an X-ray fluorescence machine at Colorado College (for both major and trace/rare earth element concentrations). To determine all elemental concentrations, hand samples taken from the flows were cut, dried, crushed, and powdered in the University of Canterbury rock sample preparation lab. For rare earth and trace element concentrations, these powders were weighed and mixed with a bonding agent at the CC lab. The resulting mixture was pressed into a disc for each sample, with all discs analyzed for trace and rare earth element concentrations by the Colorado College XRF machine. For major element concentrations, the powders were mixed with a binding agent and then melted and fused into a glass disc for each sample, all of which were again analyzed using the XRF for major oxide compositions.

Data for each sample were analyzed alongside each other and plotted with respect to their vertical and lateral positions within the Stony Bay sequence and the SB-N flow itself. Using the IgPet program, analyses were made for heterogeneities along vertical and lateral transects within the SB-N flow. The flows directly beneath SB-N and across the bay from SB-N were analyzed in order to determine the total lateral extent of the nephelinite. Geochemical values were compared to those for the Northwest Bay and East Okains Bay samples in an effort to determine any relationships among the compositions of the three primary overthickened lava flow units.

These geochemical data were complemented by the previously analyzed geochemistries of a number of samples previously analyzed at the University of Canterbury. The XRF at UC, however, was capable of determining the concentrations of a different – and smaller – set of trace and rare earth elements than the machine at CC: as a result, the discussions of lava flow chemistries in subsequent chapters focus mostly on the samples analyzed at CC. Conversely, the XRF at CC yielded somewhat less accurate values for major element concentrations than the instruments at UC, especially with regard to lighter elements such as sodium and potassium. Therefore, the major element concentrations used to calculate viscosity according to the model provided by Giordano et al. (2008) are taken from the samples analyzed at the UC lab. An additional 35 samples from the various flows in the larger Stony Bay stratigraphic sequence – that is, lava flow units stratigraphically above and below unit SB-N – were also analyzed at UC, in previous years (Eeg & Hampton, 2014) and are also considered in the results and discussion sections.

Geochemical Results

Geochemical analyses performed at the University of Canterbury lab's XRF on samples taken from East Okains Bay, Northwest Bay, and Stony Bay yielded the major oxide concentrations listed in **Table 2**.

	SiO_2	TiO_2	Al_2O_3	FeO	MnO	MgO	CaO	Na_2O	K_2O	P_2O_5
SB7	40.31	3.55	12.25	14.66	0.200	11.08	11.28	4.59	1.15	0.93
SB-AB	40.98	3.53	12.25	14.20	0.197	11.22	10.91	4.74	1.15	0.82
SB-AB2	40.11	3.59	12.36	14.46	0.199	11.41	11.13	4.80	1.11	0.84
SB-AG	40.10	3.70	12.26	14.87	0.200	10.97	11.39	4.32	1.26	0.94
NWB-14 (norm)	47.40	3.06	17.03	13.22	0.210	4.10	7.80	4.70	1.60	0.89
EO-1 (norm)	51.95	1.59	17.71	11.33	0.230	2.23	5.33	5.98	2.88	0.77

Table 2 – Major oxide concentrations for the NWB-H, SB-N, and EOB-M samples analyzed at the UC lab.

On a total alkali silica diagram from IgPet, the compositions of rocks from the Stony Bay region range from picrites to benmoreites (**Figure 8**). One might notice on this figure that the samples taken from East Okains Bay and Northwest Bay – respectively, a mugearite and a hawaiite – fall relatively well in line with the typical picrite-benmoreite Stony Bay compositional trend, which is itself like the majority of Banks Peninsula flow sequences (Hampton & Cole, 2009). This stands in stark contrast to the Stony Bay nephelinite samples, which have low silica concentrations and high alkali concentrations and thus fall well outside of the greater Banks Peninsula compositional trend.

The Harker diagrams in **Figures 9a & 9b**, respectively, plot various major element concentrations against the samples' silica concentrations for both the rough lateral and vertical transects across the SB-N flow unit. Note that, due to the limitations of the Colorado College lab's XRF when measuring concentrations of lighter elements, the results for Na_2O and, to a lesser extent, K_2O should not be taken as wholly accurate.

The lateral transect (in order from seaward to landward, samples SB2, SB3, SB4, and SB5) plotted on a Harker diagram for major element concentrations against silica concentrations (**Figure 9a**) shows no discernable or consistent pattern of heterogeneities between samples. **Figure 9b**, which does the same for minor element concentrations along our lateral transect, tells a similar story (or lack thereof). The plot of SiO_2 vs. Sc on this figure does have a trend of increasing scandium from sample SB5 to SB2 along this transect, but given how slight this

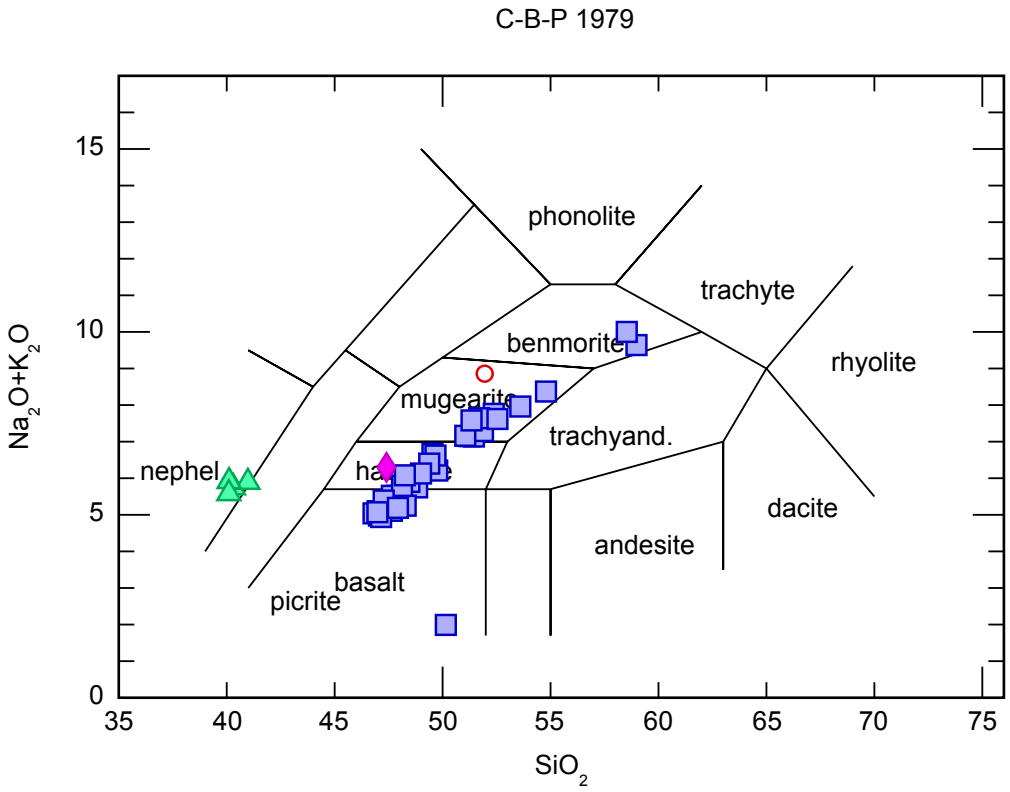

Figure 8 – Total alkali-silica (TAS) diagram for the samples collected from Stony Bay (filled green squares), East Okains Bay (red circles), and Northwest Bay (filled pink triangles) that were analyzed with the XRF at the University of Canterbury lab. Includes a number of sample geochemistries from the Stony Bay transect outside of overthickened flow unit SB-N (filled blue squares; Eeg & Hampton, 2014). Geochemistries correspond to those listed in **Table ##**. Made with IgPet.

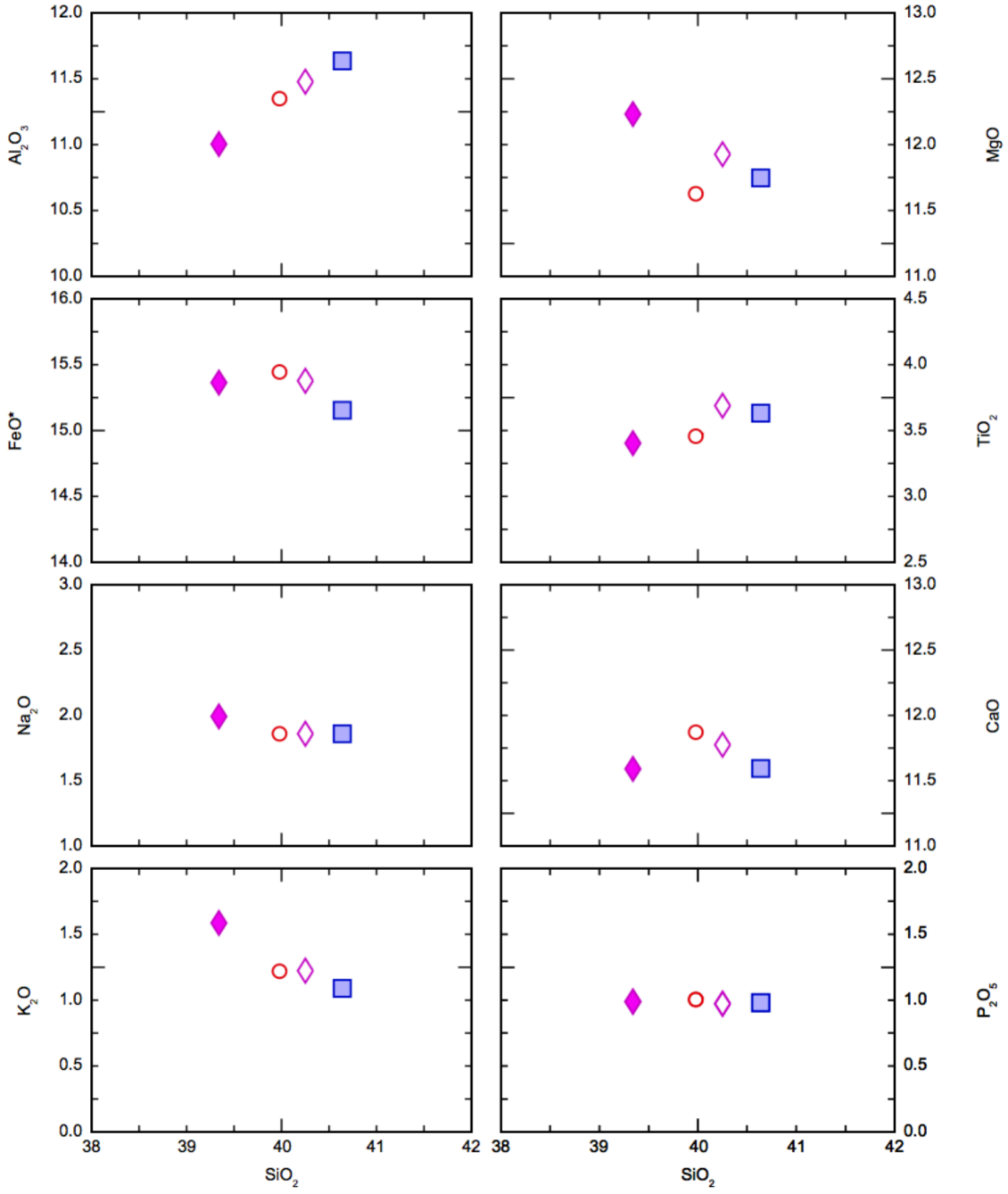

Figure 9a – Harker plots geochemistries for samples from a lateral transect along the Stony Bay flow unit SB-N (open red circle = SB5; filled pink diamond = SB4; empty pink diamond = SB3; filled blue square = SB2). **Figure 9a** plots silica concentrations against major oxide concentrations (measured as %wt). Made with IgPet.

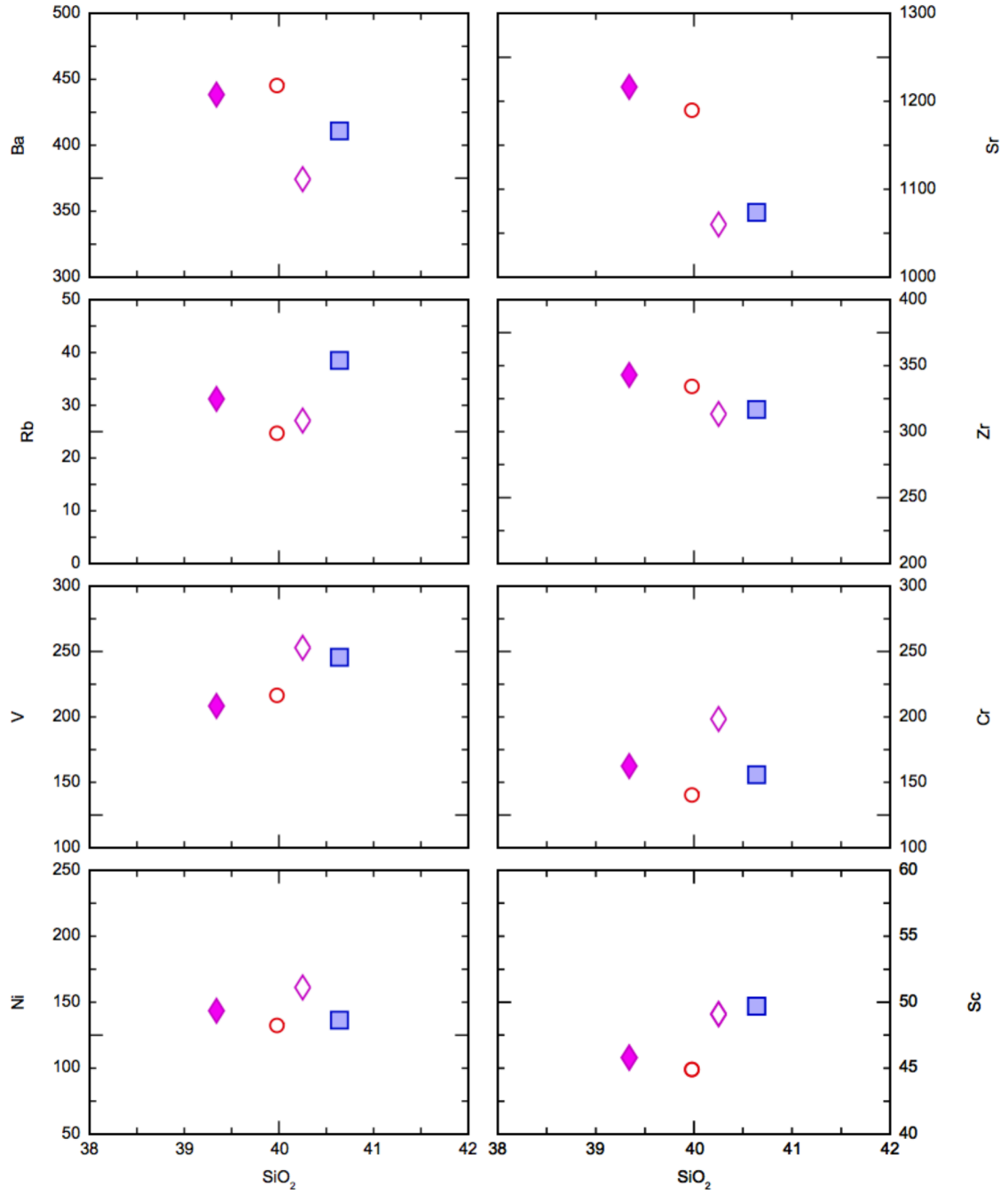

Figure 9b – Harker plots geochemistries for samples from a lateral transect along the Stony Bay flow unit SB-N (open red circle = SB5; filled pink diamond = SB4; empty pink diamond = SB3; filled blue square = SB2). **Figure 9b** plots silica concentrations against rare earth and trace element concentrations (measured in ppm). Made with IgPet.

trend is and how it shows up for no other trace elements, this trend can be disregarded.

The results are similar for the vertical transect (from the bottom to the top of lava flow unit SB-N: SB10, SB2, SB5, and SB7). There is no apparent pattern in the heterogeneities of this transect's major element concentrations (**Figure 10a**), nor in its minor and trace element concentrations (**Figure 10b**). It may be worth noting that sample SB7, taken near the top of unit SB-N, consistently displays either the lowest or highest extreme of concentrations in both Harker diagrams, which is especially apparent in some of the minor/trace element plots in **Figure 10b**. This stands out particularly the plots of SiO_2 against barium, strontium, rubidium, and zirconium. However, it is unclear what the cause of this single pattern of heterogeneity really is.

Geochemical Interpretations

An initial conclusion with regard to the research question can be drawn from the distinct rock types found from the overthickened flows at Stony Bay, Northwest Bay, and East Okains Bay (as shown in a total alkali-silica diagram in **Figure 8**). Since these three flow units display such different compositions, a strong compositional control on their unique overthickened morphologies can be ruled out. This stands opposed to some of the early hypotheses: before sampling the Northwest Bay and East Okains Bay lava flows, the only compositional information for an overthickened flow was on the Stony Bay nephelinite flow SB-N. Thus, the

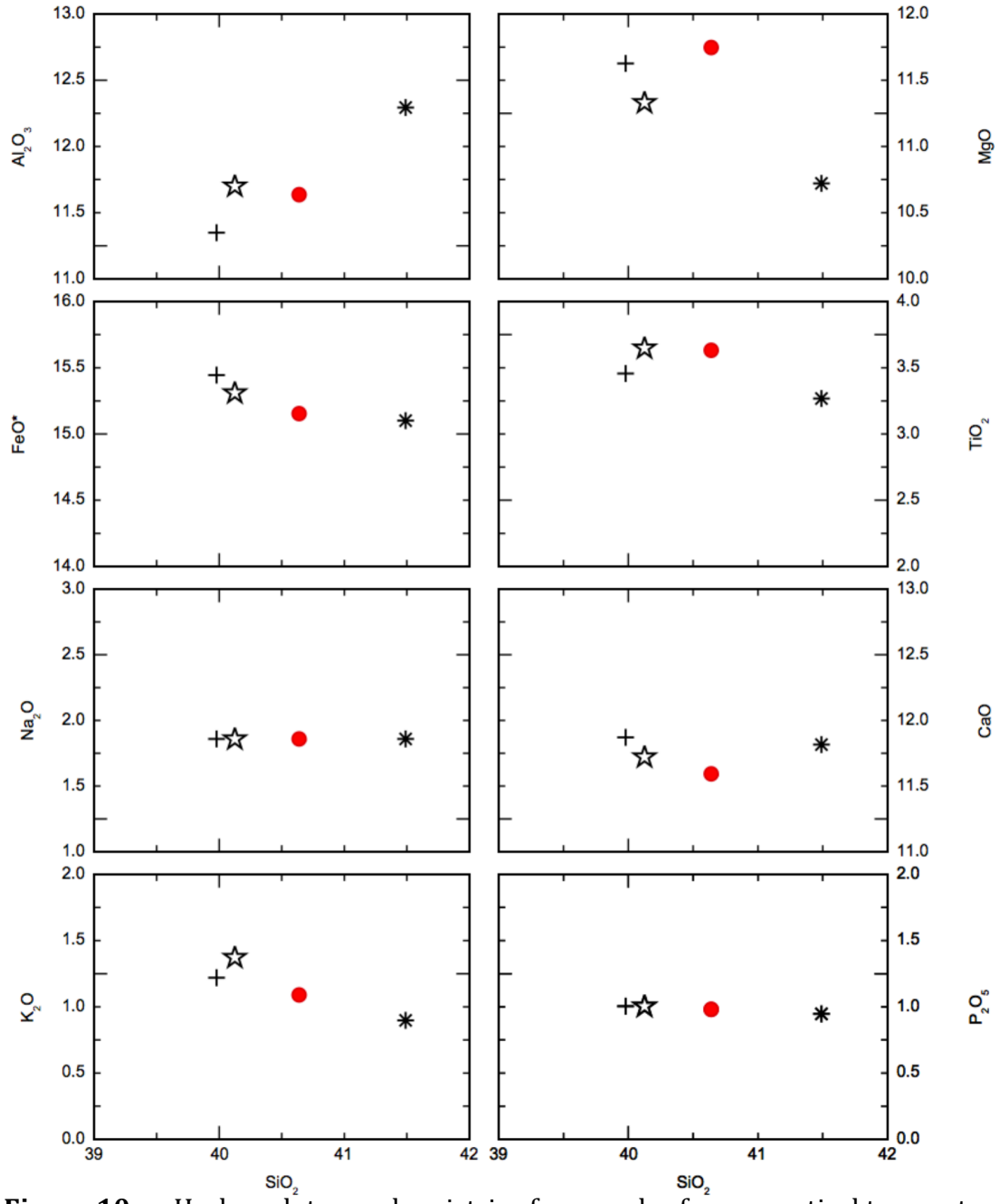

Figure 10a – Harker plots geochemistries for samples from a vertical transect along the Stony Bay flow unit SB-N (filles red circle = SB2; plus sign= SB5; asterisk = SB7; star = SB10). **Figure 10a** plots silica concentrations against major oxide concentrations (measured as %wt). Made with IgPet.

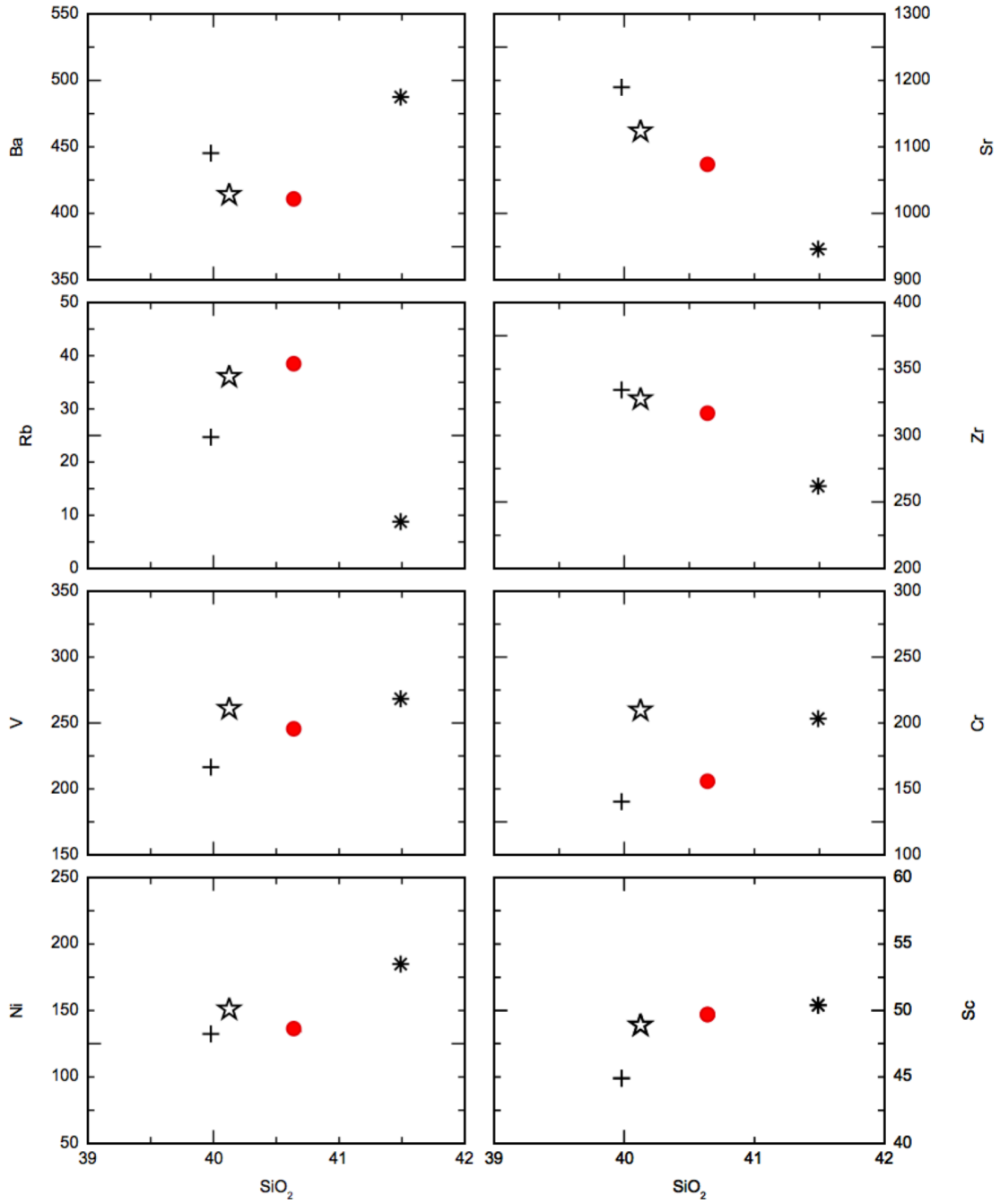

Figure 10b – Harker plots geochemistries for samples from a vertical transect along the Stony Bay flow unit SB-N (filles red circle = SB2; plus sign= SB5; asterisk = SB7; star = SB10). **Figure 10b** plots silica concentrations against rare earth and trace element concentrations (measured in ppm). Made with IgPet.

hypothesis at that point was that the two then-unsampled overthickened lava flow units may have similar compositions, pointing to a compositional control on their morphologies. However, this is not the case.

It must, however, be noted that only a single sample was collected from the East Okains Bay flow unit EOB-M due to time and accessibility constraints. This lends to significant uncertainty for this particular flow, especially relative to the primary units at Northwest Bay (NWB-H) and Stony Bay (SB-N), both of which were far more accessible and thus had a much greater number of samples collected from each than from EOB-M. It is certainly reasonable to draw the conclusion that the composition of unit EOB-M is, at the very least, significantly different from those of NWB-H and SB-N. However, it may be inadvisable to draw any more specific conclusions related to the nature of lava flow unit EOB-M with the limited data we have available on that flow.

Within the nephelinite lava flow SB-N, it can be safely concluded that there is no regular or clear pattern of lateral heterogeneity from our four-sample transect. Since the rough transects along SB-N were traversed with the intention of determining vertical rather than lateral compositional patterns, i.e. the presence, or lack thereof, of multiple discrete flows stacked atop one another in a short period of time, this is not particularly surprising.

Interestingly, the vertical transect displays a similar lack of order in its heterogeneities, both in major and minor/trace element concentrations (**Figures 10a & 10b**). If we were to take this short transect as truly representative of the entire vertical section of the overthickened flow unit SB-N, this would indicate that

the entire unit was emplaced as a single event and a single lava flow, as opposed to a series of smaller flows stacked atop each other (or, at the very least, that the hypothetical stacked flows had no significant compositional heterogeneity). It is interesting to note that the uppermost sample from SB-N (sample SB7) has consistently more extreme minor and trace element compositions than any of the other samples on this transect. However, it is not known whether this discrepancy is due to compositional heterogeneity within SB-N or simply chemical weathering of the flow. The latter is somewhat likely given that there were very few outcrops at the top of SB-N that were exposed and safely accessible.

While there was no significant compositional pattern for either the lateral or the vertical transect in SB-N, it must be noted that the transects involved only four samples each, and are, therefore, not likely representative of a complete and systematic vertical or lateral transect in this lava flow unit. The inconsistent exposure and often sheer cliff faces often found associated with this flow made it exceedingly difficult for more consistent sampling strategies to be undertaken. Future work might involve someone with rock climbing expertise who could taken a systematic vertical transect along the overthickened section of SB-N.

Additionally, plotting the geochemical results corroborate the previous conclusion that the volcanic materials in Banks Peninsula originated in an intraplate setting (**Figures 11a & 11b**). Both figures use immobile elements that do not usually migrate during weathering and therefore likely represent the original setting of the flows.

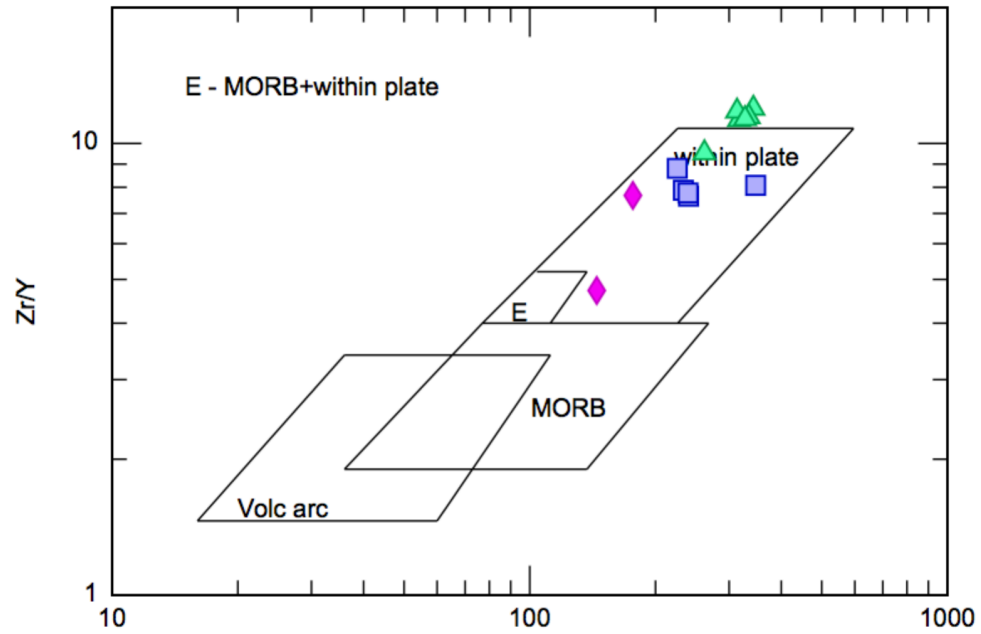

Figure 11a

Figure 11b

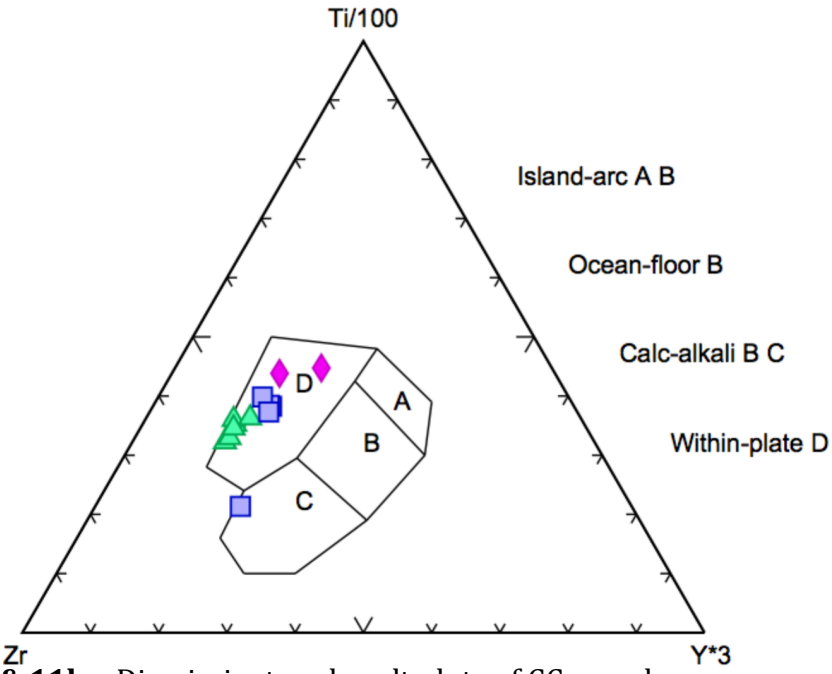

Figures 11a & 11b – Discriminatory basalt plots of CC sample geochemistries. **Figure 11a** plots Zr vs. Zr/Y, from Pearce & Norry, 1979. **Figure 11b** plots Zr, Y^3, and Ti/100 on a ternary diagram, from Pearce & Cann, 1973. Pink diamonds are NWB-H hawaiites, green triangles are Sb-N nephelinites, and blue squares are other Stony Bay samples. Made with IgPet.

Chapter 6 – Temperature Modeling

Temperature Methods

MELTS is a thermodynamic modeling software program first developed by Ghiorso & Sack (1995), with derivatives that include programs pMELTS, rhyolite-MELTS, and others. It was built to provide an interface through which users can investigate melting and crystallization in natural magmatic systems (Gualda & Ghiorso, 2015). The most recent iteration of this software, MELTS_Excel, is meant to rectify the GUI-style interface of previous versions, which was sometimes cumbersome for novice users (Gualda & Ghiorso, 2015). For this study, MELTS_Excel is used to calculate liquidus temperatures and mass fractionation curves for the samples taken from the three field locations.

Temperature Results

Any temperature estimates obtained using the MELTS software should be somewhat similar to observed temperatures from basalt flows. There are very few specific temperature ranges given for specific varieties of basalt flows, and those that are given overlap with each other significantly. Due to the composition's relative uniqueness, estimates for nephelinites are more readily available than they are for hawaiites or mugearites. Platz et al. (2004) put forward a range of 1100-1170 °C based on studies of nephelinites erupted from Nyiragongo Volcano, with Gee & Sack (1988) and Sawyer et al. (2008) providing similar estimates. Bultitude & Green (1967) provide maximum eruption temperatures ranging from 1250 °C to

1370 °C, depending on the flow's volatile concentration. Less specific data is available for hawaiites and mugearites, but the more general estimate for basaltic temperatures of 1000-1250 °C seems reasonable in their case (Kilburn, 2000).

Running each of the 14 sample compositions analyzed with the Colorado College lab's XRF, along with the five samples analyzed with the University of Canterbury's XRF, and using MELTS for Excel yielded liquidus temperatures at a pressure of 1 MPa (**Table 3**) (Gualda & Ghiorso, 2015). The reasoning for choosing the 1 MPa pressure value is explained in the following "Significance" section. **Figure 12** illustrates the relationship between the liquidus temperatures calculated by MELTS and silica concentrations of the samples. Volatile content was set at 0.1% due to the MELTS Excel sheet vastly overcalculating melt liquidus temperatures when running completely anhydrous data sets. Based on typical values for low-silica melts (Sawyer et al., 2008), a low volatile concentration added to the model still allows the spreadsheet to function properly without corrupting the data and results.

There is an obvious, and expected, correlation between higher silica content and lower liquidus temperatures in **Figure 12**. The nephelinite samples – six from the Colorado College lab's XRF and four from the University of Canterbury lab's XRF – are tightly clustered together. Higher silica flows – mostly hawaiites falling in the 47-49% SiO_2 range – are clustered to an extent, but less tightly than the nephelinite samples. The former range from a minimum of 1155 ˚C to a maximum of 1230 ˚C, while the more tightly clustered, higher temperature nephelinites range from 1254 ˚C to 1290 ˚C with an average of approximately 1270 ˚C. This difference in clustering

Sample ID	%SiO_2	Liquidus T (˚C) at 1 Mpa
BPSB4	39.34	1290.03
BPSB5	39.979	1277.54
SBAG	40.1	1254.1
SB2AB	40.11	1258.4
BPSB10	40.125	1273.05
BPSB3	40.251	1280.08
SB7	40.31	1254.49
BPSB2	40.639	1276.37
SBAB	40.98	1257.81
BPSB7	41.49	1267.58
NWB2	45.761	1229.88
NWB1a	46.702	1200.78
BPSB9	47.284	1169.73
NWB14	47.4	1155.27
BPSB12	47.542	1172.07
BPSB8	47.808	1180.66
BPSB6	47.925	1175.59
BPSB11	49.031	1156.64
EO1	51.95	1141.6

Table 3 – Liquidus temperatures [˚C] at 1 MPa for CC samples (NWB1a & 2, BPSB2-12) and UC samples (SB7, AG, AB, 2AB; NWB14; & EO1). Red text denotes samples analyzed at the UC lab; all others analyzed at the CC lab. Temperatures calculated using MELTS (Gualda & Ghiorso, 2015)

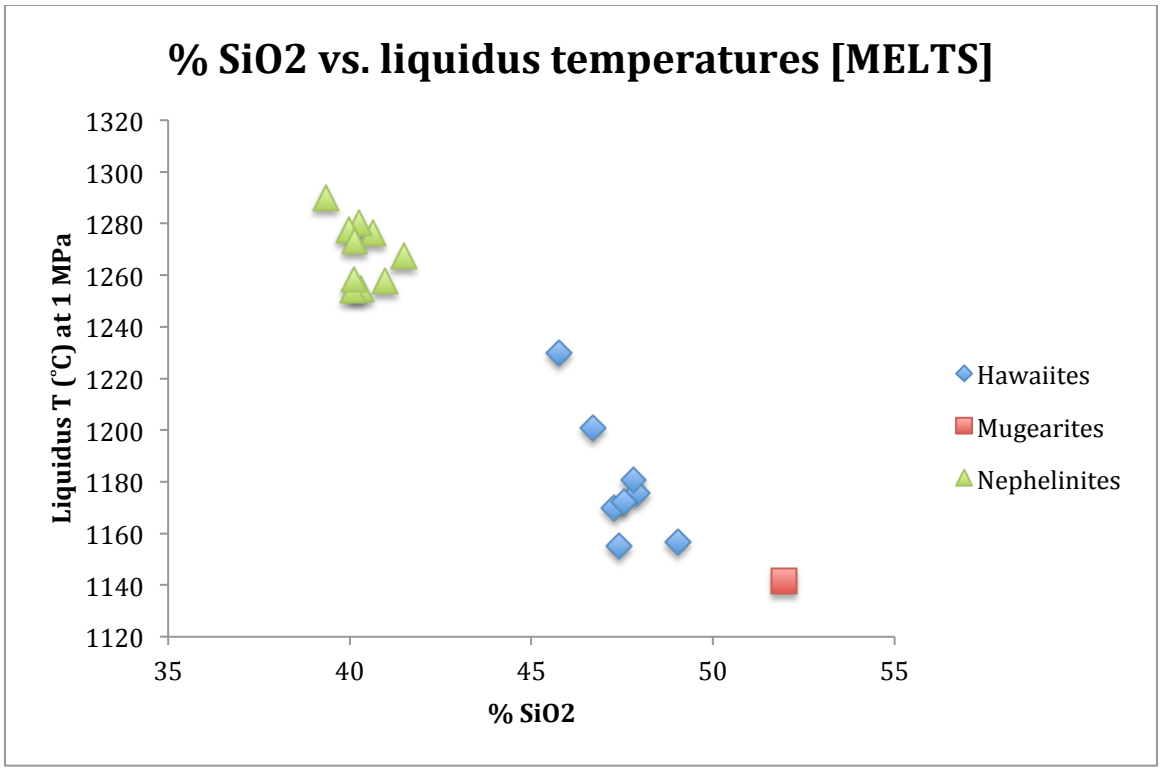

Figure 12 – $\%SiO_2$ vs. liquidus temperatures [˚C] at 1 MPa for a selection of hawaiites, mugearites, and nephelinites from the great Stony Bay geochemical sequence. Created using MELTS (Gualda & Ghiorso, 2015).

is likely due to the fact that all nephelinite samples were taken from one lava flow unit, while the hawaiites include samples from both the Northwest Bay flow and a number of hawaiite units throughout the greater Stony Bay flow succession. The lone mugearite sample has a calculated liquidus temperature of 1142 ˚C, which is, as expected, the lowest of all calculated values (given that higher-silica melts have lower liquidus temperatures).

Fractionation curves are presented in Figure 13, assuming a pressure of 1 MPa and temperatures between 100 and 1400 ˚C. A pressure of 1 MPa was chosen because it was reasonably close to the pressures that the flows might presumably experience at the surface under their own weight. I chose to run the model only for samples SB4 and NWB2a as representative samples from the nephelinite and hawaiite populations that would be sufficient for the model. The lone mugearite sample, from East Okains Bay, was not considered for these calculations given that the larger sample sizes of the Northwest Bay and Stony Bay data sets made them better candidates for study. Additionally, limited accessibility at the East Okains Bay lava flow unit in question, EOB-M, meant that the only attainable sample was from an outcrop of a much greater degree of physical and chemical weathering than were the samples from Stony Bay and Northwest Bay. Therefore, we determined that it might be unsafe to draw any specific conclusions based on the one East Okains Bay mugearite sample beyond very generalized statements about the nature of the bays' compositions.

In the fractionation curve displayed in **Figure 13**, the relationship between the phases of various minerals and their temperatures is outlined. The primary

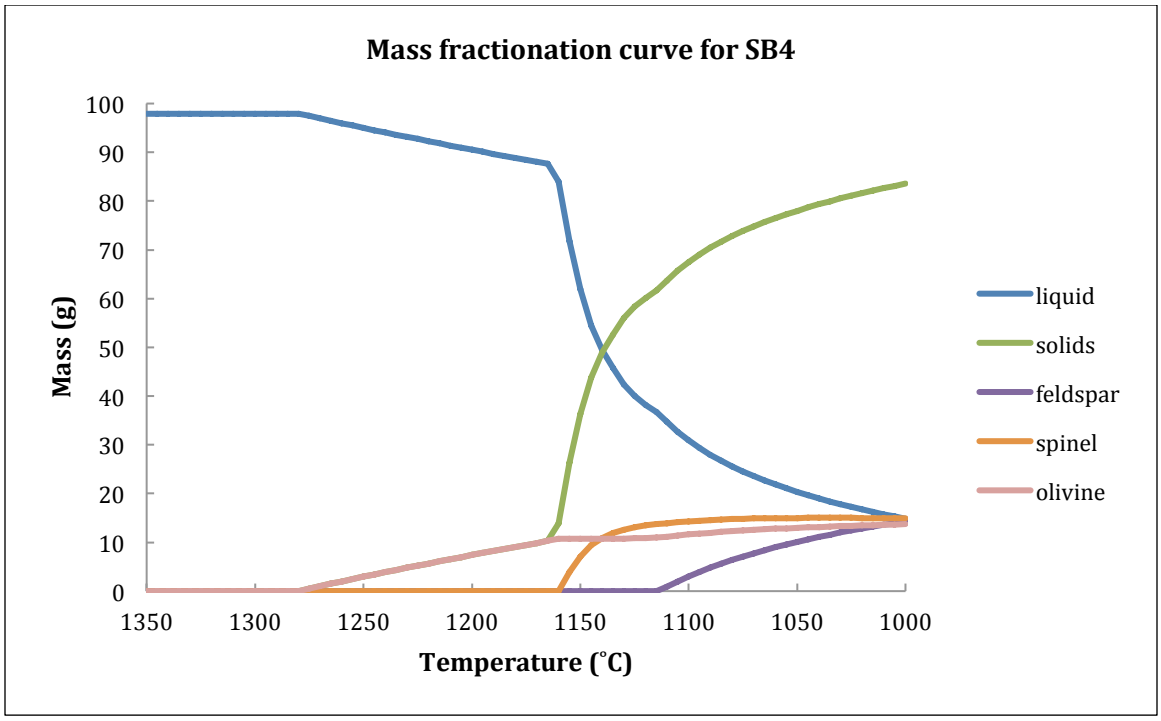

Figure 13 – Mass fractionation curve for Stony Bay nephelinite sample SB4. Created using the MELTS program (Gualda et al., 2012).

curve is the blue liquid trend, which begins at 100% mass and decreases gradually as the melt cools until it hits the point at which spinel begins to fractionate along with olivine, when it begins to rapidly descent with temperature. At the same time, the overall mass percentage of solids rapidly increases. If this calculation had been carried out past 1000 ˚C, liquid mass percentages would have eventually fallen to zero and solids to 100%.

Temperature Interpretations

Analyses of the geochemistries of each sample using MELTS serve to narrow the range of temperatures over which viscosities will be estimated using the model crafted by Giordano et al. (2008). These data for liquidus temperatures define a new maximum estimated temperature for the nephelinite flow SB-N of approximately 1270 ˚C, based on averaging the liquidus temperatures calculated for all nephelinite samples. If the liquidus temperature of a melt is taken to represent the temperature at which the melt begins to crystallize solids, then a melt that erupted as a lava flow at or above its liquidus temperature would, theoretically, have no phenocrysts. Since even the most aphanitic lava flows in this study display small percentages of solids, it is interpreted that liquidus temperatures to represent maximum possible temperatures of eruption.

Furthermore, these model results may have some use in inferring not only the *maximum* possible eruption temperatures – assumed to match the compositions' liquidus temperatures – of the flows in question, but also their *exact* eruptive temperatures. The fractionation curves (**Figure 13)** may be combined with

petrographic data such that a measurement of the net crystallinity of the nephelinite thin sections may approximate the proportion of solid materials in the melt during eruption and emplacement. Thus, the observed solid/liquid ratio is matched to the proper point on the MELTS fractionation curves and traced to its corresponding temperature, to obtain a more precise and plausible estimate of lava flow temperatures.

The most significant issue in these estimates is that the MELTS program runs into issues when calculating fractionation curves and liquidus temperatures at pressures beneath 1 MPa (10 bar). Given that standard atmospheric pressure is approximately 1 bar, the minimum possible pressure of 10 bar for these MELTS calculations is significantly greater than the true pressure these flows would have been subjected to. This could lead to errors in using values calculated by MELTS as described.

As a test of this method, **Figure 13** displays a mass fractionation curve calculated for sample SB4, from the overthickened nephelinite flow SB-N. Petrographic observations of this sample indicate a crystal percentage of approximately 7%, largely consisting of olivine and plagioclase phenocrysts with occasional opaques and very rare clinoyroxenes. Such a melt consists of approximately 7% solid material at a temperature of 1220 ˚C, an approximate eruptive temperature for this flow. This estimate of eruption temperatures will be used to help determine viscosities and effusion rates.

Chapter 7 – Viscosity Modeling

Viscosity Methods

The approach used in this section relies on the mathematical modeling of lava flow viscosities described previously in **Chapter 3** (Giordano et al., 2008). An Excel-based version of this model is used (**Figure 14**), into which the samples' major oxide concentrations (as determined via XRF analyses) were entered, along with a range of temperatures over which the model calculated its results, yielding an output of predicted viscosities at each temperature for each sample concentration. The results from the MELTS calculations (**Table 4, Fig. 15** & **16**) constrain temperature ranges more tightly than the generalized temperature ranges given in the literature for various lava geochemistries.

Viscosity Results

Model results for lava viscosity suggests a strong correlation between a flow's composition, particularly its silica concentration, and its viscosity (Gualda & Ghiorso, 2015; Giordano et al., 2008). Evidence for this logarithmic relationship between viscosity and temperature is presented in **Figure 15**, which plots flow viscosity against temperature for the averaged compositions of overthickened flow units SB-N and NWB-H. For any given temperature, viscosity estimates are noticeably higher for a Northwest Bay hawaiite than it is for a Stony Bay nephelinite, and viscosity also increases with lower temperatures, meaning that a very low-temperature hawaiite will have a far higher viscosity than a very high-temperature

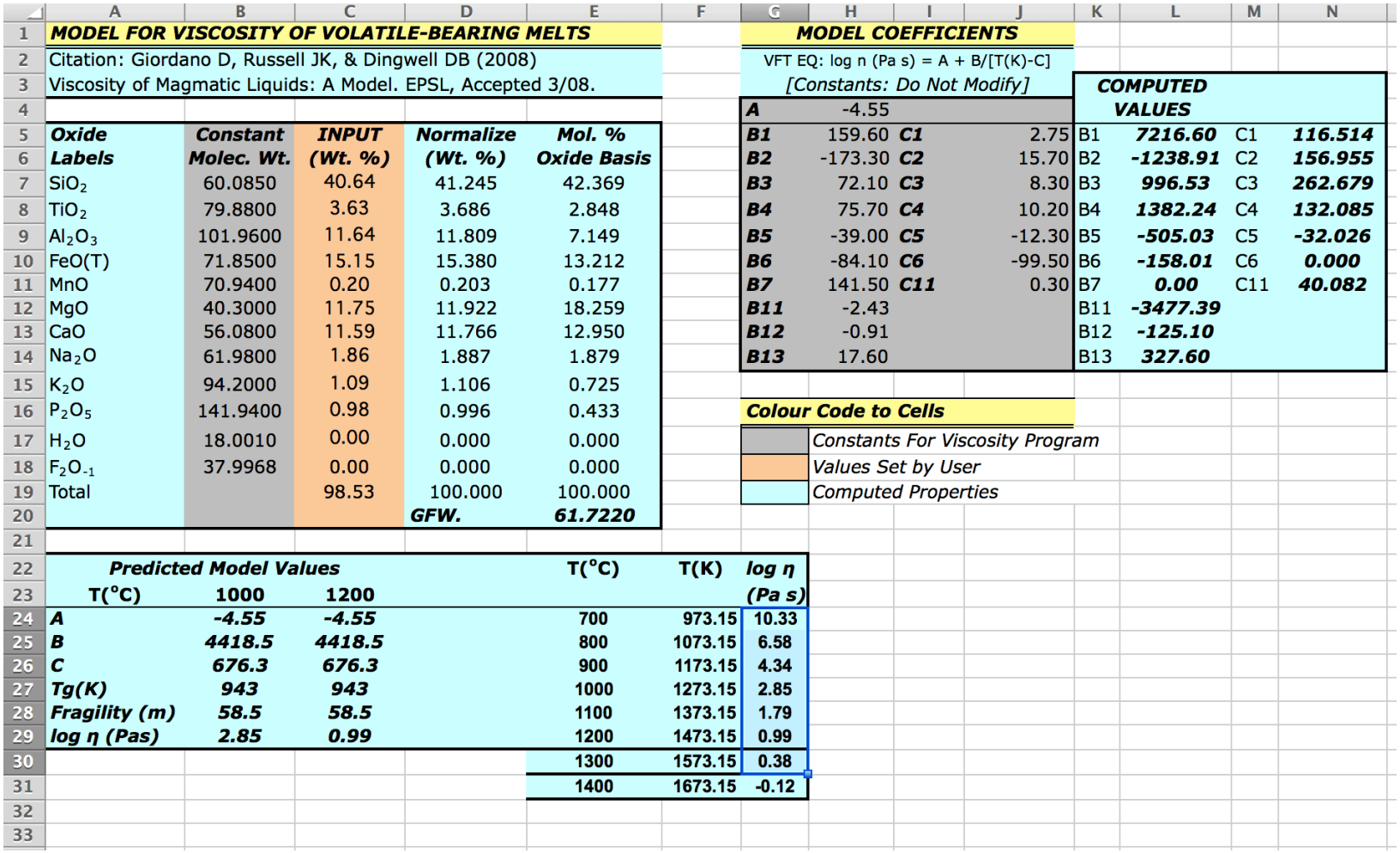

MODEL FOR VISCOSITY OF VOLATILE-BEARING MELTS

Citation: Giordano D, Russell JK, & Dingwell DB (2008)
Viscosity of Magmatic Liquids: A Model. EPSL, Accepted 3/08.

Oxide Labels	Constant Molec. Wt.	INPUT (Wt. %)	Normalize (Wt. %)	Mol. % Oxide Basis
SiO_2	60.0850	40.64	41.245	42.369
TiO_2	79.8800	3.63	3.686	2.848
Al_2O_3	101.9600	11.64	11.809	7.149
FeO(T)	71.8500	15.15	15.380	13.212
MnO	70.9400	0.20	0.203	0.177
MgO	40.3000	11.75	11.922	18.259
CaO	56.0800	11.59	11.766	12.950
Na_2O	61.9800	1.86	1.887	1.879
K_2O	94.2000	1.09	1.106	0.725
P_2O_5	141.9400	0.98	0.996	0.433
H_2O	18.0010	0.00	0.000	0.000
F_2O_{-1}	37.9968	0.00	0.000	0.000
Total		98.53	100.000	100.000
			GFW.	61.7220

MODEL COEFFICIENTS

VFT EQ: log n (Pa s) = A + B/[T(K)-C]
[Constants: Do Not Modify]

A	-4.55			B1	7216.60	C1	116.514
B1	159.60	C1	2.75	B2	-1238.91	C2	156.955
B2	-173.30	C2	15.70	B3	996.53	C3	262.679
B3	72.10	C3	8.30	B4	1382.24	C4	132.085
B4	75.70	C4	10.20	B5	-505.03	C5	-32.026
B5	-39.00	C5	-12.30	B6	-158.01	C6	0.000
B6	-84.10	C6	-99.50	B7	0.00	C11	40.082
B7	141.50	C11	0.30	B11	-3477.39		
B11	-2.43			B12	-125.10		
B12	-0.91			B13	327.60		
B13	17.60						

Colour Code to Cells

	Constants For Viscosity Program
	Values Set by User
	Computed Properties

Predicted Model Values			T(°C)	T(K)	log η
T(°C)	1000	1200			(Pa s)
A	-4.55	-4.55	700	973.15	10.33
B	4418.5	4418.5	800	1073.15	6.58
C	676.3	676.3	900	1173.15	4.34
Tg(K)	943	943	1000	1273.15	2.85
Fragility (m)	58.5	58.5	1100	1373.15	1.79
log η (Pas)	2.85	0.99	1200	1473.15	0.99
			1300	1573.15	0.38
			1400	1673.15	-0.12

Figure 14 – A screenshot of the Excel spreadsheet version of the Giordano et al. (2008) viscosity model. This particular example is the model run for sample SB-2.

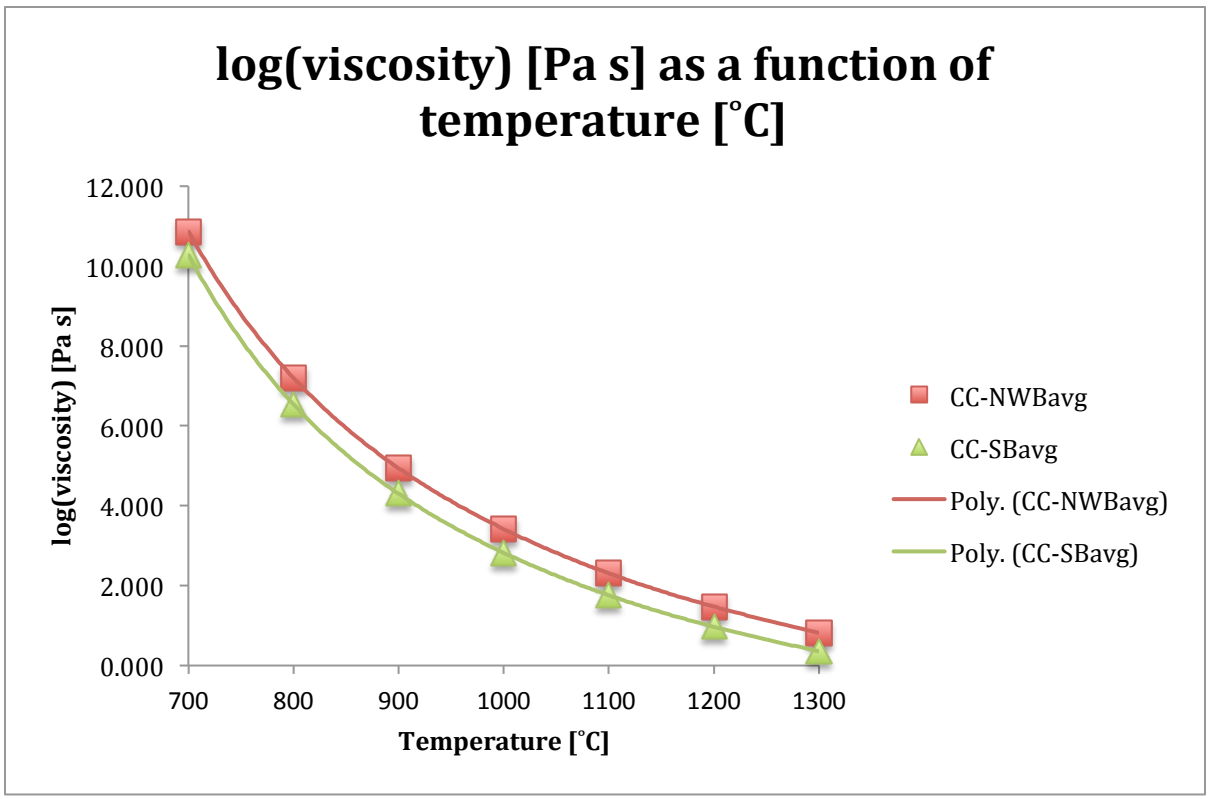

Figure 15 – log(viscosity) [Pa s] as a function of temperature [˚C] for the averaged geochemistries of all nephelinites taken from flow unit SB-N and hawaiites from flow NWB-H analyzed at the CC lab. Based on the Giordano et al. (2008) viscosity model.

nephelinite. Values were calculated on a 100 ˚C interval from 700 ˚C to 1300˚C. **Table 4** lists exact viscosity values for each temperature for the averaged geochemistries of the six SB-N nephelinite samples and that of the two NWB-H hawaiite samples.

Figure 16 presents the results of the model as run for all geochemistries throughout the entire Stony Bay flow sequence, as a means of illustrating the relationship between viscosity and geochemistry. This was done by averaging the major oxide concentrations for all samples of each rock type on a picrite-benmoreite sequence of Stony Bay flows; all samples here were from previous research and were analyzed at the University of Canterbury lab. The relationship between temperature and viscosity is logarithmic, with viscosity exponentially increasing as temperature decreases. This matches observations from the previous MELTS model runs. It is apparent that for any single temperature there can easily be multiple orders of magnitude of difference between lower- and higher-silica endmembers – discounting the nephelinite – of the Stony Bay sequence (respectively, picrite and benmoreite).

Viscosity Interpretations

A number of test runs were performed with the Giordano et al. model in order to determine the sensitivity to change in various input parameters that could be viewed as problematic (Giordano et al., 2008). The first of these focus on the presence, or lack thereof, of water within the samples. As explained in the previous

T [˚C]	T [K]	η_SBavg [Pa s]	η_NWBavg [Pa s]
1000	1273.15	659.97	1360.80
1025	1298.15	333.50	705.43
1050	1323.15	177.66	383.31
1075	1348.15	99.19	217.25
1100	1373.15	57.74	127.89
1125	1398.15	34.90	77.91
1150	1423.15	21.81	48.96
1175	1448.15	14.06	31.65
1200	1473.15	9.31	20.99
1225	1498.15	6.33	14.25
1250	1523.15	4.40	9.89
1275	1548.15	3.12	7.00
1300	1573.15	2.26	5.04

Table 4 – Exact viscosity values [Pa s] for each temperature between 1000 ˚C and 1300 ˚C on 25 ˚C increments for averaged SB-N and NWB-H compositions. Calculations done according to Giordano et al., 2008.

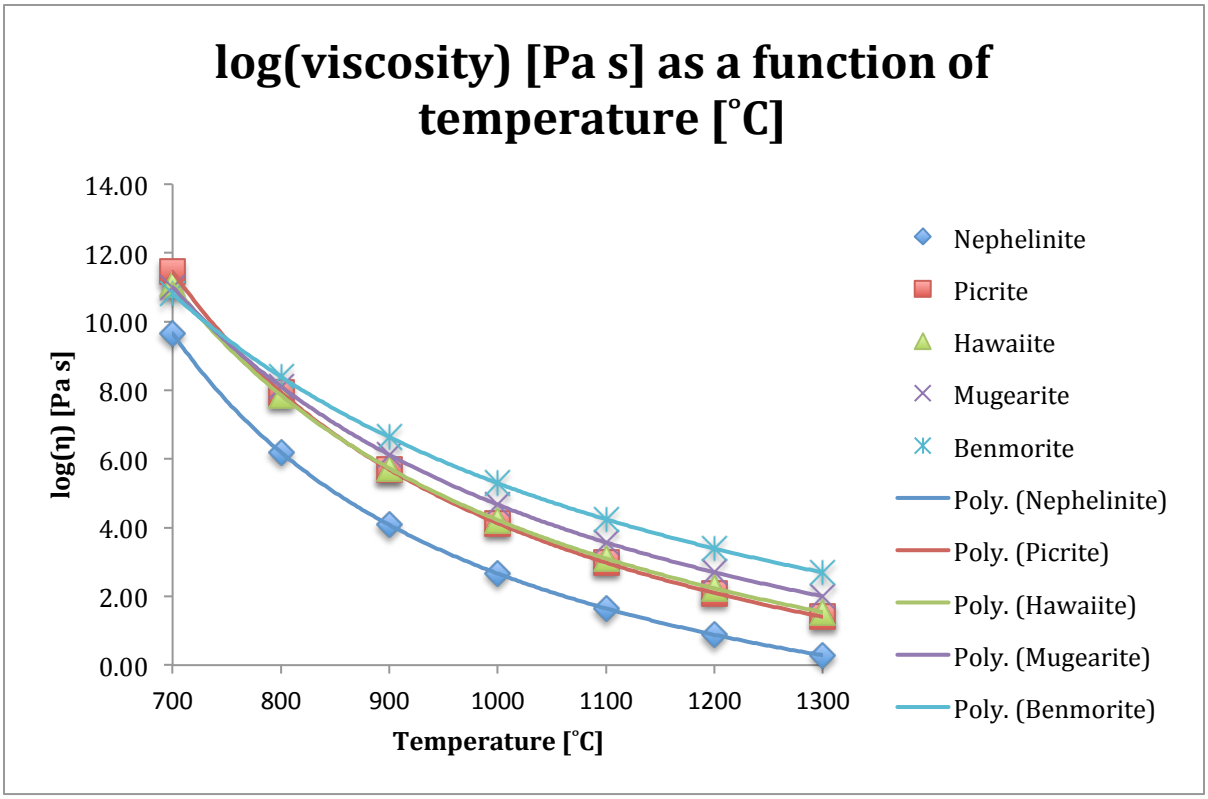

Figure 16 – log(viscosity) [Pa s] as a function of temperature [˚C] for the averaged geochemistries of all lava types along the greater Stony Bay flow sequence, ranging from low-silica picrites and nephelinites to high-silica benmoreites. All samples analyzed with the UC lab's XRF, and all were from previous research (Eeg & Hampton, 2014).

chapters, sample geochemistries were all necessarily anhydrous, and even at the time of emplacement it is safe to assume that the lava flows in question had very low volatile contents (especially for the very low-silica nephelinite flows). However, since volatile contents are certainly very strong influences on the viscosity of a lava flow, it is prudent determine the effect of water on the viscosity calculations. I did this by adding an H_2O content of 0.1% to the sample geochemistries and calculating new values in the Giordano model. The 0.1% value was chosen because, when running the MELTS model in an attempt to increase the precision of the flow temperature estimates, an H_2O content of 0.1% was required for the model to run properly.

Figure 17 presents a plot of the results for both the anhydrous viscosities and those with an added 0.1% H_2O content for the averaged geochemistries of the overthickened flow units NWB-H and SB-N. **Table 5** gives exact values for these new calculations for SB-N, along with quantifications of the error generated by these results. Viscosity is shown to consistently decrease with an added 0.1% H_2O content, sometimes significantly. The decrease is much greater for lower temperatures than it is for higher temperatures: for example, calculating the viscosity of an anhydrous and a hydrous SB-N sample at 1300 ˚C yields a drop of only 20.12% from the former to the latter (respectively, from 2.26 to 1.80 Pa s), while doing the same calculation for a sample at 700 ˚C sees a 92.10% drop in viscosity (from $1.88*10^{10}$ to $1.49*10^{9}$ Pa s).

The eruptive temperatures of the nephelinite flow are very unlikely to have been below around 1050 ˚C, with rough MELTS calculations suggesting a

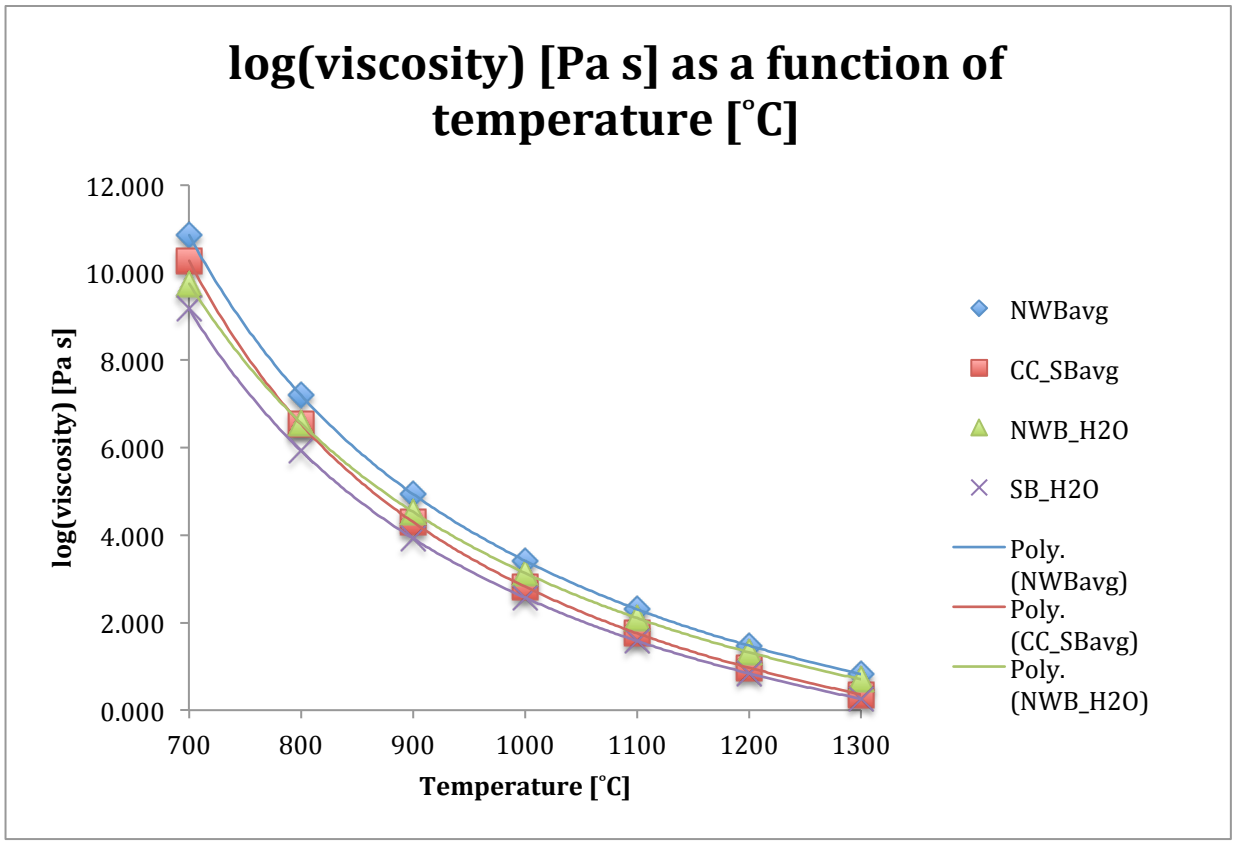

Figure 17 – log(viscosity) [Pa s] as a function of temperature [˚C] for the averaged geochemistries of all SB-N nephelinite samples and NWB-H hawaiite samples, both for anhydrous geochemistries and hydrous (+0.1% H_2O) geochemistries. Samples analyzed with the CC lab's XRF. Based on the Giordano et al. (2008) viscosity model.

T [˚C]	T [K]	η (ahydrous) [Pa s]	η (hydrous) [Pa s]	% decrease anhydrous to hydrous
700	973.15	1.88E+10	1.49E+09	92.10%
800	1073.15	3.44E+06	8.54E+05	75.16%
900	1173.15	2.01E+04	8.49E+03	57.80%
1000	1273.15	659.97	370.54	43.86%
1100	1373.15	57.74	38.43	33.44%
1200	1473.15	9.31	6.91	25.78%
1300	1573.15	2.26	1.80	20.12%

Table 5 – Comparison of viscosity values [Pa s] calculated for hydrous (+0.100% H_2O) and anhydrous (0% H_2O) geochemistries for the averaged SB-N compositions. Calculations according to Giordano et al, (2008).

temperature closer to 1200 ˚C or 1300 ˚C. Given the imprecision of many of these quantities throughout this study, an error on this scale, translating to roughly ± 10-15%, seems reasonable.

An additional source of possible uncertainty is the difference between the calculated results for the samples analyzed at the University of Canterbury lab and those analyzed at the Colorado College lab. The larger sample size available for the CC nephelinite samples makes them more desirable for in-depth analyses. However, the CC lab energy dispersive XRF does a poor job with calculating Na_2O concentrations, giving rise to concerns about exclusively using the CC samples for viscosity analyses. To check this margin, viscosity values calculated for the averaged CC nephelinite sample geochemistries were plotted against those calculated for the averaged UC nephelinite samples. The result is shown in **Figure 18** and in **Table 6**. Similar to the error associated with the presence, or lack thereof, of H_2O in the samples, the error increases for lower temperatures when comparing viscosity values calculated for UC and CC values. Like with before, this is due to the viscosity model being more sensitive to changes in $\%SiO_2$ at lower temperatures. CC samples are associated with slightly higher viscosities across the board, but the margin of error is even less than that calculated for the anhydrous vs. hydrous samples, with only a 14.50% difference between the averaged CC and UC samples at 1300 ˚C.

The viscosity-temperature plots span temperatures from 700 ˚C to 1300 ˚C as a means of fully displaying the logarithmic relationship between the two parameters. When analyzing these data for usable viscosity values, we can ignore the values that fall below 1000 ˚C, since a brief review of the literature indicates that

T [˚C]	T [K]	η (UC) [Pa s]	η (CC) [Pa s]	% decrease CC to UC
700	973.15	4.589E+09	1.884E+10	75.65%
800	1073.15	1.551E+06	3.439E+06	54.90%
900	1173.15	1.209E+04	2.012E+04	39.94%
1000	1273.15	463.252	659.969	29.81%
1100	1373.15	44.534	57.743	22.88%
1200	1473.15	7.636	9.314	18.01%
1300	1573.15	1.930	2.257	14.50%

Table 6 – Comparison of viscosity values [Pa s] calculated for the averaged geochemistries of the CC SB-N samples and the UC SB-N samples. Calculations according to Giordano et al, (2008).

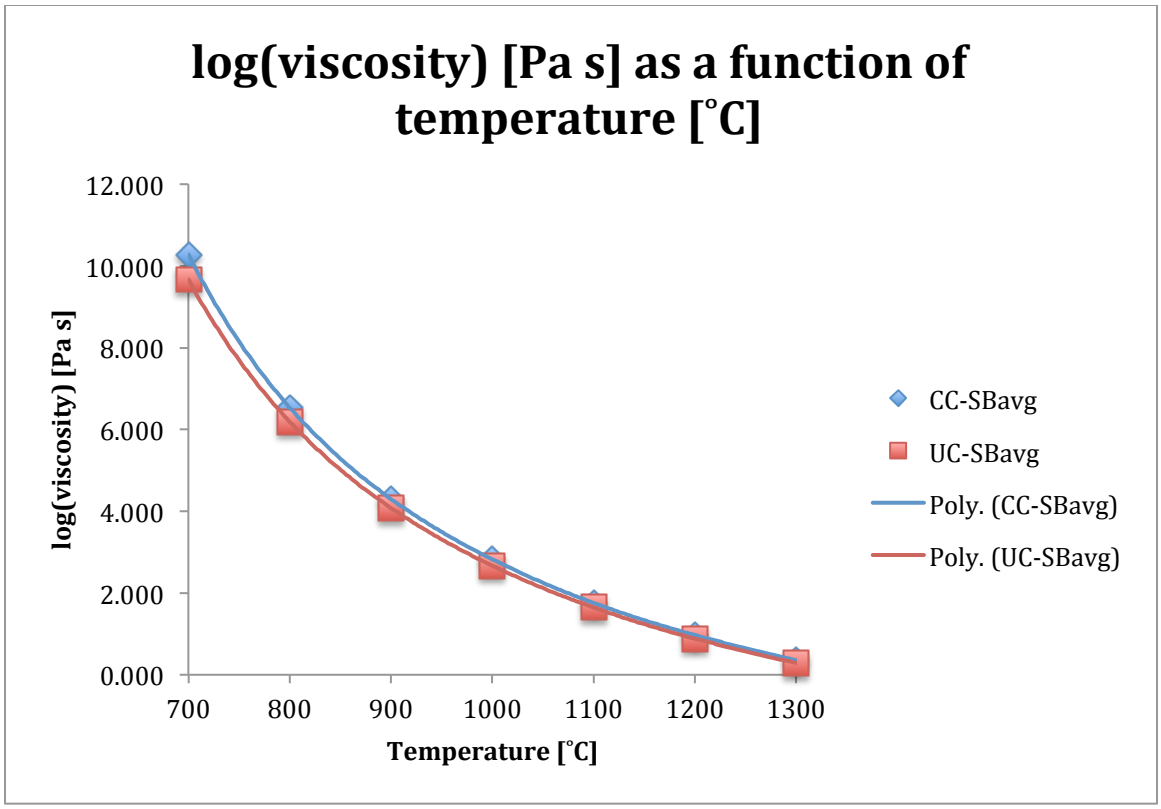

Figure 18 – log(viscosity) [Pa s] as a function of temperature [˚C] for the averaged geochemistries of all SB-N nephelinite samples and NWB-H hawaiite samples, split into samples analyzed by the CC lab's XRF and those analyzed by the UC lab's XRF. Based on the Giordano et al. (2008) viscosity model.

nephelinite and hawaiite temperatures are not likely to fall below that during eruption (as outlined in Chapter 6, this literature review provides a window of between 1000 ˚C and 1250 ˚C for reasonable nephelinite eruption temperatures). Additionally, the approximate liquidus temperature of 1270 ˚C calculated with the MELTS program further narrows down this window of viable temperatures to the upper range of those determined from the literature. Due to the relatively minor influence of a possible small volatile content we effectively exclude this from further calculations. Thus, our final temperature range of approximately 1150 ˚C to 1250 ˚C is taken to provide the best estimates for the viscosity of the nephelinite flow immediately following eruption (refer back to **Table 4**).

Chapter 8 – Effusion Rate Modeling

Effusion Rate Methods

The techniques used for calculating effusion rates for the overthickened lava flow units are built on the mathematical models of effusion rates previously described in Chapter 3, provided by Tallarico et al. (2006). Given the dimensions of the flows in question (discounting the anomalously thick sections of the flows), the two-dimensional Bingham rheology is the most appropriate configuration for calculating these flows' effusion rates.

A configurable version of this model was made by transcribing the relevant equations into Wolfram Mathematica. While the impacts of adjusting most parameters is examined, the primary focus is on the effects of flow thickness and flow viscosity on effusion rates. Determining moderately precise estimates of effusion rate was certainly a goal in this final phase of our study. However, as with viscosity, the uncertainties associated with many of the quantifiable parameters in the Tallarico et al. (2006) effusion rate model when applied to old and weathered lava flow units meant that it was also necessary to consider the assumptions and possible variations in parameters that might affect the calculations. Rather than producing precise estimates from these calculations, a range of plausible values is a more reasonable outcome.

Dimensional values needed for the model such as flow thickness and flow width were based on observations of the overthickened units in sections upslope from the overthickened sections in an attempt to keep the calculations for these flows consistent with those for more morphologically standard flows throughout

Banks Peninsula. Flow widths were, in particular, very difficult to accurately quantify due to erosion and vegetation obscuring their true lateral extents. Thus, a great deal of uncertainty presents itself in these results. A similar situation arose regarding the thicknesses of the flows (flow heights), although a few moderately well exposed sections of the NWB-H and SB-N flows increase the certainty of this input variable.

Effusion Rate Results

Figure 19 displays a plot of effusion rate as a function of flow viscosity for flow thicknesses on 0.25 m increments from 0.5 m to 4.0 m, while **Figure 20** plots effusion rate as a function of flow thickness for viscosities between 10 Pa s and 2000 Pa s (Tallarico et al., 2006). **Table 7** presents a specific set of effusion rate values for various combinations of reasonable flow thicknesses and viscosities, corresponding to the graphs in **Figures 19 & 20**. **Appendix A** contains a more detailed table of effusion rate values based on flow thicknesses and flow viscosities.

Worth noting are the exceptionally large changes in effusion rate corresponding to minor variations in flow thickness and viscosity. Lower viscosity values and higher flow thicknesses invariably correspond to a large increase in effusion rates. For example, a low viscosity combined with a high flow thickness will produce an effusion rate that is orders of magnitude greater than that derived from a high viscosity combined with a low flow thickness. For example, at a viscosity of 50 Pa s, a flow thickness of 1.0 m results in an effusion rate (1391 $m^3 s^{-1}$) over eight

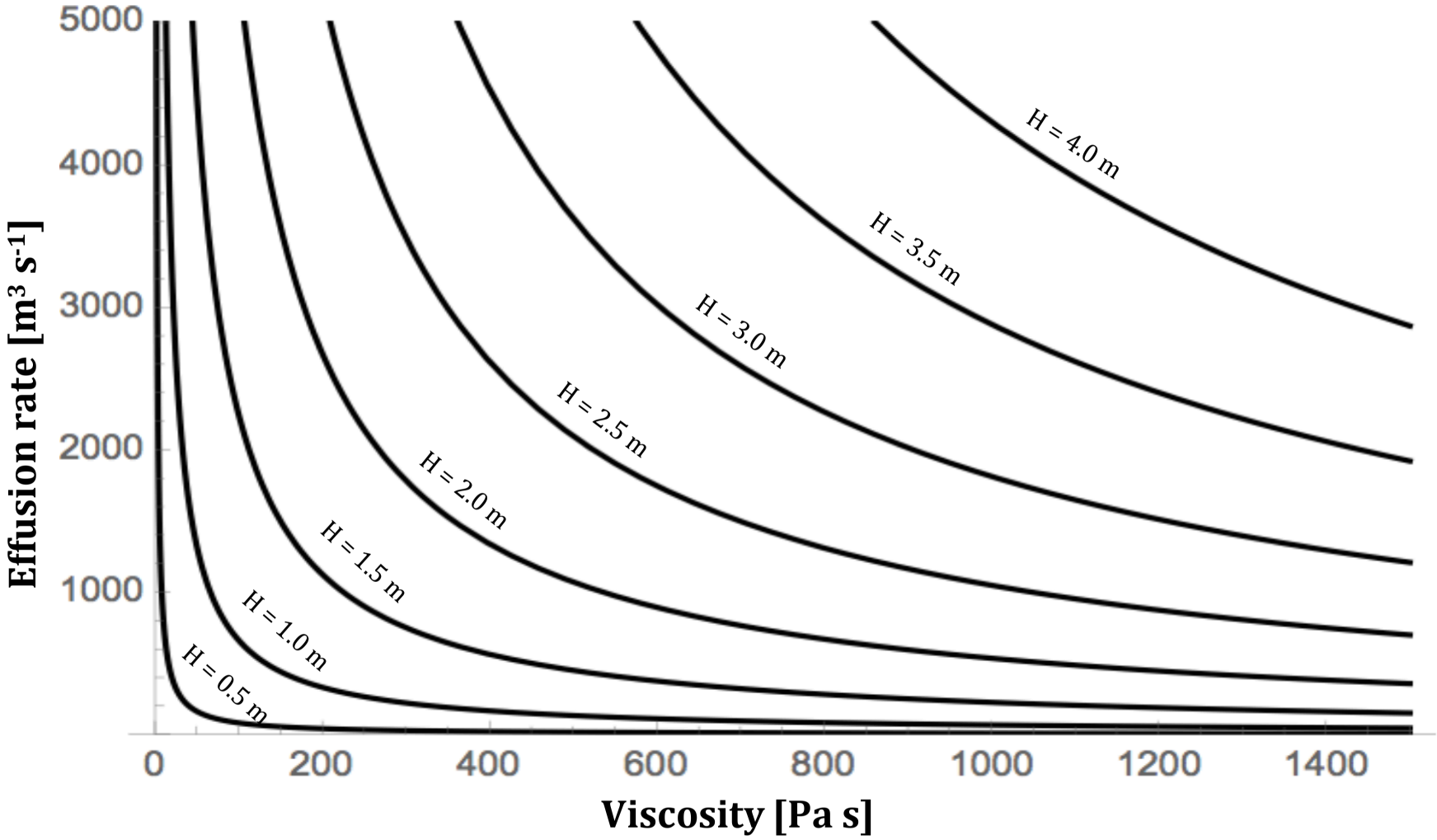

Figure 19 – A plot of viscosity [Pa s] vs. effusion rates [m^3 s^{-1}] with respect to flow heights in increments of 0.5 m. Calculations done according to Tallarico et al. (2006).

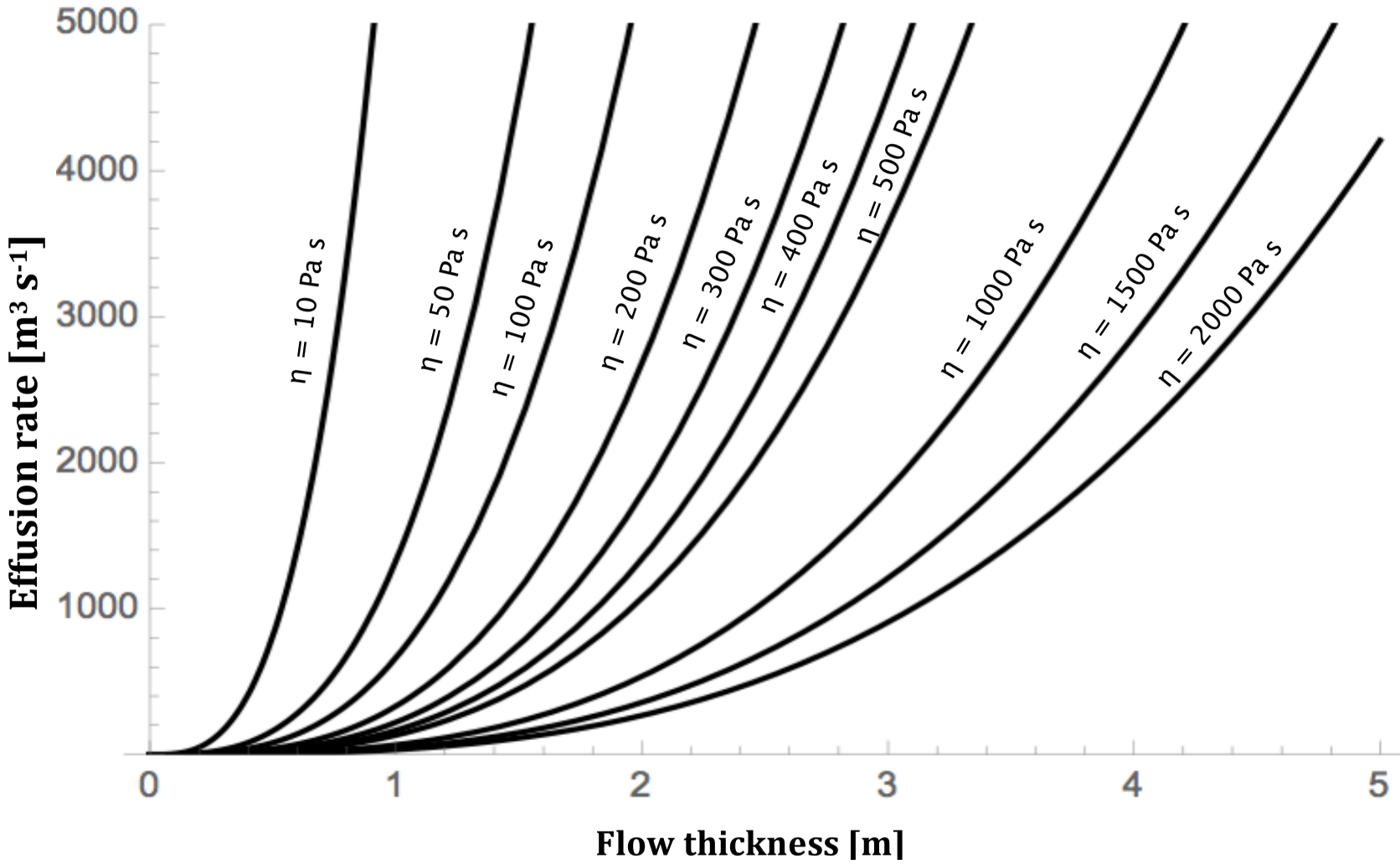

Figure 20 – A plot of Flow thickness [m] vs. effusion rate [m^3 s^{-1}] with respect to viscosities from 10-2000 Pa s. Calculations done according to Tallarico et al. (2006).

	H = 0.5 m	H = 1.0 m	H = 1.5 m	H = 2.0 m	H = 40 m
μ = 50 Pa s	170.6 $m^3 s^{-1}$	1391 $m^3 s^{-1}$	4726 $m^3 s^{-1}$	11240 $m^3 s^{-1}$	$9.07x10^8$ $m^3 s^{-1}$
μ = 100 Pa s	85.30 $m^3 s^{-1}$	695.7 $m^3 s^{-1}$	2363 $m^3 s^{-1}$	5618 $m^3 s^{-1}$	$4.54x10^7$ $m^3 s^{-1}$
μ = 250 Pa s	34.12 $m^3 s^{-1}$	278.3 $m^3 s^{-1}$	945.1 $m^3 s^{-1}$	2247 $m^3 s^{-1}$	$1.81x10^7$ $m^3 s^{-1}$
μ = 500 Pa s	17.06 $m^3 s^{-1}$	139.1 $m^3 s^{-1}$	472.6 $m^3 s^{-1}$	1124 $m^3 s^{-1}$	$9.07x10^6$ $m^3 s^{-1}$

Table 7 – Effusion rates [$m^3 s^{-1}$] calculated from a range of viscosities [Pa s] and flow thicknesses [m]. Calculations done according to Tallarico et al. (2006).

times as high as that calculated at a thickness of 0.5 m (170.6 m^3 s^{-1}). This rapid exponential increase in effusion rates with flow thickness is also made evident in the values given in **Table 7** for a 40 m thickness, roughly corresponding to the thickest sea cliff sections of the two overthickened flow units SB-N and NWB-H. These values range from millions (at 500 Pa s) to hundreds of millions (at 50 Pa s) of cubic meters per second.

Effusion Rate Interpretations

Relationships between flow thickness and effusion rate and between flow viscosity and effusion rate are highly sensitive to small changes in their respective independent variables. As displayed in **Figures 19 and 20**, after reaching a low enough viscosity or a large enough flow thickness, the rate of increase in effusion rate rises dramatically. This means that combination of a high flow thickness with a low viscosity results in an unrealistically large value for effusion rate. For example, according to the two-dimensional Bingham model for flow rheology, a flow thickness of 4.0 combined with a viscosity of 25 Pa s – with flow width being kept constant at 40 m – results in an effusion rate of 180,636 m^3 s^{-1}, which is orders of magnitude above the maximum possible effusion rates for ordinary basaltic flows (Tallarico et al., 2006).

Among the myriad uncertainties associated with the quantitative analysis of the rheologies of these overthickened flows, flow width was one of the most significant. The sensitivity of width as an independent variable to the dependent

effusion rate variable is similar to that of viscosity and flow height. In an attempt to simplify these calculations and analyses, a constant flow width value of 40 m – approximated for relatively large sections of the Northwest Bay overthickened flow unit NWB-H using Google Earth – was used for all effusion rate calculations. It was decided that effort would be better spent analyzing the effect of flow thickness and viscosity on effusion rate outputs, given that precision for those independent variables was significantly greater than it was for flow widths.

One solid conclusion to be drawn from these estimated effusion rates is that effusion rates could not have been the sole control on the morphology of the abnormally thick flows. This conclusion is reached using the Tallarico et al. (2006) model to calculate the effusion rate of a flow with a thickness of 40 m (approximately what the NWB-H and SB-N flows averaged in their thickest sections). Referring to **Table 7**, we can see that the effusion rate outputs for these model runs are in the realm of hundreds of thousands of cubic meters per second, reaching over a million $m^3\ s^{-1}$ in the case of the lower-viscosity runs. Previous research indicates that effusion rates for basalt flows can range from $< 1\ m^3\ s^{-1}$ up to $\sim 8500\ m^3\ s^{-1}$, the latter in the case of a large fissure eruption like that of the 1783 fissure eruption of Laki in Iceland, the latter of which may be equivalent to a minor flood basalt event (Thordarson & Self, 1993). The effusion rates calculated by the model as necessary for a continuous 40 m-thick lava flow are up to three orders of magnitude beyond the highest known value for a non-flood basalt lava flow. Thus, since necessary effusion rates for these thicknesses would be close to physically impossible to achieve, we can conclude that the thickest morphologies of the flow

units in Northwest Bay and Stony Bay could not be solely a product of high effusion rates. Furthermore, these results may point to an emplacement of the SB-N and NWB-H lava flow units that involved multiple discrete flows being erupted on top of one another in relatively quick succession.

Chapter 9 – Discussion

Model Errors

Various errors associated with the steps involved in the process of this study have been touched upon in each chapter, but yet to be discussed is how they carry through to the end products of the quantitative models used for viscosity and effusion rate. Of the variables carrying the bulk of these errors, some, such as the influence of paleo-topography on the morphology of the flows at the time of emplacement (again, roughly mid-late Miocene), are not strictly quantifiable, rendering any attempts to detail their error somewhat useless. Other factors, such as mass crystal fractions (and other variables in the Tallarico et al. (2006) effusion rate models), would theoretically be quantifiable but for a lack of the requisite time, knowledge, and resources.

Therefore, efforts to quantify uncertainties and errors in this chapter, especially with regard to their influence on estimates of viscosities and effusion rates are focused on those variables throughout different steps of this process that can feasibly be quantified. Of these, the most important may be the 3-5% error associated with the XRF analyses' silica percentages (a preliminary analysis of their effect on viscosity calculations, as per Giordano et al. (2008), can be found in Chapter 7) and the huge uncertainties associated with field dimensions, especially flow widths and thicknesses. A preliminary analysis of certain aspects of the former and their influence on viscosity calculations, as per Giordano et al. (2008), can be found in Chapter 7, while some discussion of the latter can be found in the effusion rate analyses in Chapter 8.

In order to quantify the effect of a ±3% error in the XRF geochemical analyses on our results (see **Chapter 5**), for simplicity's sake, I will carry this error through all steps of this study while holding other variables constant. Focus will remain entirely on SiO_2 percentages, which have a far greater effect on flow rheologies than the other major oxide percentages that were measured. Taking the geochemistry of hawaiite flow unit NWB-H (based on an average of samples NWB-1 and NWB-2) as a working example, with an initial calculated $\%SiO_2$ of 46.23%, we obtain a range of 44.84% to 47.62 % for ±3%. Plugging this into the Giordano et al. (2008) viscosity model yields the results displayed in **Table 8** for a select range of temperatures on 50 ˚C intervals.

Due to the difficulty of using the MELTS program to calculate accurate temperatures for low-pressure surface flows (see Chapter 6), using a rough estimate for flow temperature of 1100 ˚C seems to be a reasonable assumption for our purposes. Therefore, a ±3% error in the geochemistry of the average NWB-H hawaiite flow results in a minimum viscosity of 102.33 Pa s and a maximum viscosity of 158.49 Pa s (Giordano et al., 2008). With the midpoint viscosity of 128.82 Pa s, this range translates to -20.56% for the minimum result and +23.03% for the maximum result. Thus, translating the ±3% error found in the geochemistry step to the step following geochemistry – viscosity calculations – multiplies the initial percent error by a factor of approximately 7.

The next, and final, step in this rough evaluation of the implications of a ±3% error in $\%SiO_2$ on the calculations in the final stages of this study is to carry the approximately ±21% viscosity margin of error through to the Tallarico et al. (2006)

Flow T	%SiO_2_-3%	%SiO_2_norm	%SiO_2_+3%
1100 ˚C	102.33 Pa s	128.82 Pa s	158.49 Pa s
1150 ˚C	39.81 Pa s	48.98 Pa s	60.26 Pa s
1200 ˚C	16.98 Pa s	20.89 Pa s	25.70 Pa s
1250 ˚C	8.13 Pa s	10.00 Pa s	12.02 Pa s

Table 8 – Viscosities calculated (using Giordano et al., 2008) over a range of temperatures from the averaged NWB-H %SiO_2 ±3%.

effusion rate models. The flow width will be set at 30 m, so as to maintain the focus of this process solely on the uncertainty associated with viscosity. Results are calculated on 0.5 m flow thickness intervals, and are displayed below in **Table 9**.

For all the flow thickness values in **Table 9**, the effusion rates calculated using the -20.56% viscosity (102.33 Pa s) are approximately 25.90% greater than those for the standard viscosity (128.82 Pa s). Effusion rates calculated with the +23.03% viscosity (158.49 Pa s) were all approximately 18.72% lower than the standard viscosity effusion rates. This translates to a margin of error of ±22.31% for effusion rates calculated from a viscosity whose margin of error was ±21.80%. This increase in the margin of error from viscosity to effusion rate is somewhat negligible compared to the sevenfold increase between the geochemistry and effusion rate steps. Therefore, the majority of the error rooted in the initial ±3% margin of error in the silica content calculated by the CC lab's XRF is a result of relatively minor variations in silica content exerting disproportionately significant control on the results calculated by the Giordano et al. (2008) model for lava flow viscosities.

Discounting some of the unrealistically high effusion rate values in **Table 9** for the 1.5 m and 2 m flow thicknesses, the error itself (a margin of approximately 22%), while certainly not negligible, is within reason given the nature of quantifying such specific parameters for such old, poorly-exposed, and eroded lava flow units. If this were the sole major source of uncertainty throughout this study, it would be entirely possible to determine a somewhat reasonable range of values for effusion rate. However, just as the initial ±3% error in the $\%SiO_2$ was compounded with each successive calculation, the convergence of multiple such sources of error over the

Flow thickness	visc_-20.56%	visc_norm	visc_+23.03%
0.5 m	62.52 $m^3 s^{-1}$	49.66 $m^3 s^{-1}$	40.36 $m^3 s^{-1}$
1 m	509.89 $m^3 s^{-1}$	405.01 $m^3 s^{-1}$	329.19 $m^3 s^{-1}$
1.5 m	1731.72 $m^3 s^{-1}$	1375.62 $m^3 s^{-1}$	1118.10 $m^3 s^{-1}$
2 m	4117.8 $m^3 s^{-1}$	3271.03 $m^3 s^{-1}$	2658.68 $m^3 s^{-1}$

Table 9 – Effusion rates calculated (using Tallarico et al., 2006) over a range of flow thicknesses from the viscosities in **Table 8** at 1100 ˚C.

course of these measurements and calculations presents a serious issue. Each source of error and uncertainty builds upon each other until, by the time effusion rate calculations are undertaken, this study is left with a cumulative margin of error greatly exceeding ±22%.

One of the most egregious of these compounding uncertainties is the flow width variable in the Tallarico et al. (2006) effusion rate models. Flow widths can result in extremely large margins of error in the final effusion rate calculations even with somewhat minor variations in flow widths. This is an especially serious problem when considering how poorly-exposed, variable, and eroded the flows themselves are, making accurate estimates of flow width very difficult to come by in this study. For example, keeping all else equal (viscosity = 500 Pa s, flow thickness = 2.0 m), the model calculates an effusion rate of 1123.66 $m^3 s^{-1}$ for a flow width of 40 m, and an effusion rate of 983.21 $m^3 s^{-1}$ for a flow width of 35 m. This translates to a 12.5% decrease in effusion rate for the same percent decrease in flow width, ignoring the fact that the uncertainty inherent in the flow width variable is likely far greater than 5 m.

Now, combine the geochemical/viscosity uncertainty of approximately ±22% with a flow width uncertainty of approximately ±12.5%. Refer back to **Table 9** to find the minimum and maximum effusion rate values possible between these two variables' margins of error. The results of these quick calculations are presented below in **Table 10**. All calculations are done with a constant flow thickness of 2 m.

Thus, combining the maximum and minimum viscosities for this test with the maximum and minimum flow widths yields a minimum effusion rate value of 2215.6

	visc_-20.56% = 102.33 Pa s	**visc_+23.03% = 158.49 Pa s**
width_-12.5% = 25 m	3431.5 $m^3 s^{-1}$	2215.57 $m^3 s^{-1}$
width_+12.5% = 35 m	4804.1 $m^3 s^{-1}$	3101.79 $m^3 s^{-1}$

Table 10 – Effusion rates calculated (using Tallarico et al., 2006) over the minimum and maximum viscosity and flow width values according to the margins of error calculated for those variables above.

$m^3\ s^{-1}$ and a maximum of 4804.1 $m^3\ s^{-1}$. With a midpoint of 3509.9 $m^3\ s^{-1}$, this translates to a margin of error of approximately ±37%. With the uncertainty of each other crucial variable successively taken into account (especially flow thickness, flow slope, flow temperatures, and less easily quantifiable variables such as plug height), this margin of error will continue to increase, leading to the conclusion that any attempt at calculating a somewhat precise range of values for the effusion rates required to emplace these overthickened flow units will largely result in a dearth of satisfying results.

Aside from silica content, the variable that will most affect the viscosity results and, thus, the effusion rates is lava flow temperature. Temperature is significantly more difficult to quantify precisely and accurately we can perform a quick analysis of a margin of error similar to what was just done for geochemistry. Here, we take a midpoint of 1150 ˚C, a minimum of 1050 ˚C, and a maximum of 1250 ˚C (translating to ±100 ˚C, or ±8.7%), which seems to be a reasonable margin of error given how poorly constrained the temperature estimates have been. Using the average NWB-H silica content of 46.23% as a midpoint, we obtain a midpoint of 48.98 Pa s, a minimum of 10.00 Pa s (-79.6%), and a maximum of 380.19 Pa s (+676%). This, after calculating an exact midpoint of 195 Pa s, translates to a margin of error of ±94.9%.

Finally, we combine the margins of error associated with $\%SiO_2$ (±3% becomes ±22%) and flow temperature (±8.9% becomes ±94.9%) to obtain a cumulative margin of error for flow viscosity. The results are displayed below in **Table 11**.

	%SiO2_-3% = 44.84%	%SiO2_+3% = 47.62%
temp_-8.9% = 1050 ˚C	301.00 Pa s	478.63 Pa s
temp_+8.9% = 1250 ˚C	8.13 Pa s	12.022 Pa s

Table 11 – Viscosities calculated (using Giordano et al., 2008) over the minimum and maximum temperature and $\%SiO_2$ values according to the margins of error previously calculated for those variables.

With a minimum viscosity value of 8.13 Pa s (maximum temperature + minimum %SiO_2) and a maximum of 478.63 Pa s (minimum temperature + maximum SiO_2), we obtain an averaged midpoint of 243.38 Pa s. This yields a margin of error of ±96.7%. This is a slight increase over the margin of error of the temperature alone.

Another major error analysis that will further outline the significant issues with uncertainties in the effusion rate models is for flow thickness. Its relationship to flow viscosity is similar to the relationship between viscosity and flow width but for the fact that flow thicknesses are significantly smaller than widths and, thus, are much more affected by relatively minor variations in thickness. Again, calculations are performed according to the two-dimensional Bingham rheology model from Tallarico et al. (2006). For the sake of convenience, the same approximately ±22% margin of error used for viscosity in the previous error analyses is again used here. A 30 m flow width was used.

The margin of error for flow thickness is approximately 0.5 m, translating to ±25% with a midpoint of 2.0 m. While this is a somewhat smaller uncertainty than was given for flow widths due to the comparative ease of obtaining slightly more precise measurements of flow thicknesses in the field, the percentage itself is larger because of how low the values for flow thicknesses usually are in comparison to those for flow widths. Additionally, there is a significant amount of variability in flow thicknesses laterally throughout the flow. This held especially true for the overthickened flow units NWB-H and SB-N, both of which gradually thinned out travelling laterally landward along the flow. For both flows, exposures disappeared

or were rendered inaccessible before their upslope thicknesses completely stabilized, further contributing to the relatively large margin of error for flow thicknesses.

Combining the margins of error for viscosity and flow thickness yields the values displayed in **Table 12**, with a minimum effusion rate of 1118.1 $m^3 s^{-1}$ and a maximum of 8057.8 $m^3 s^{-1}$. With a midpoint of 4588.0 $m^3 s^{-1}$, this translates to a margin of error of nearly ±76%. Given the exponential relationship between viscosity and effusion rate, this will be different for other flow thicknesses, but it shows how much uncertainty there is in the final effusion rate calculations as a result of combining uncertainties from viscosities and flow thicknesses. This zone of possible values is displayed below as the red zone in **Figure 21**.

Once we factor the effect of a ±94.9% margin of error for viscosity based on a ±8.9% margin of error for temperature into these calculations, this zone of possible effusion rate values grows significantly. The requisite minimum and maximum values are displayed in **Table 13** below, using the same ±25% flow thickness as before. This new range of viscosities and consequent effusion rate results is marked as the blue zone in **Figure 21**.

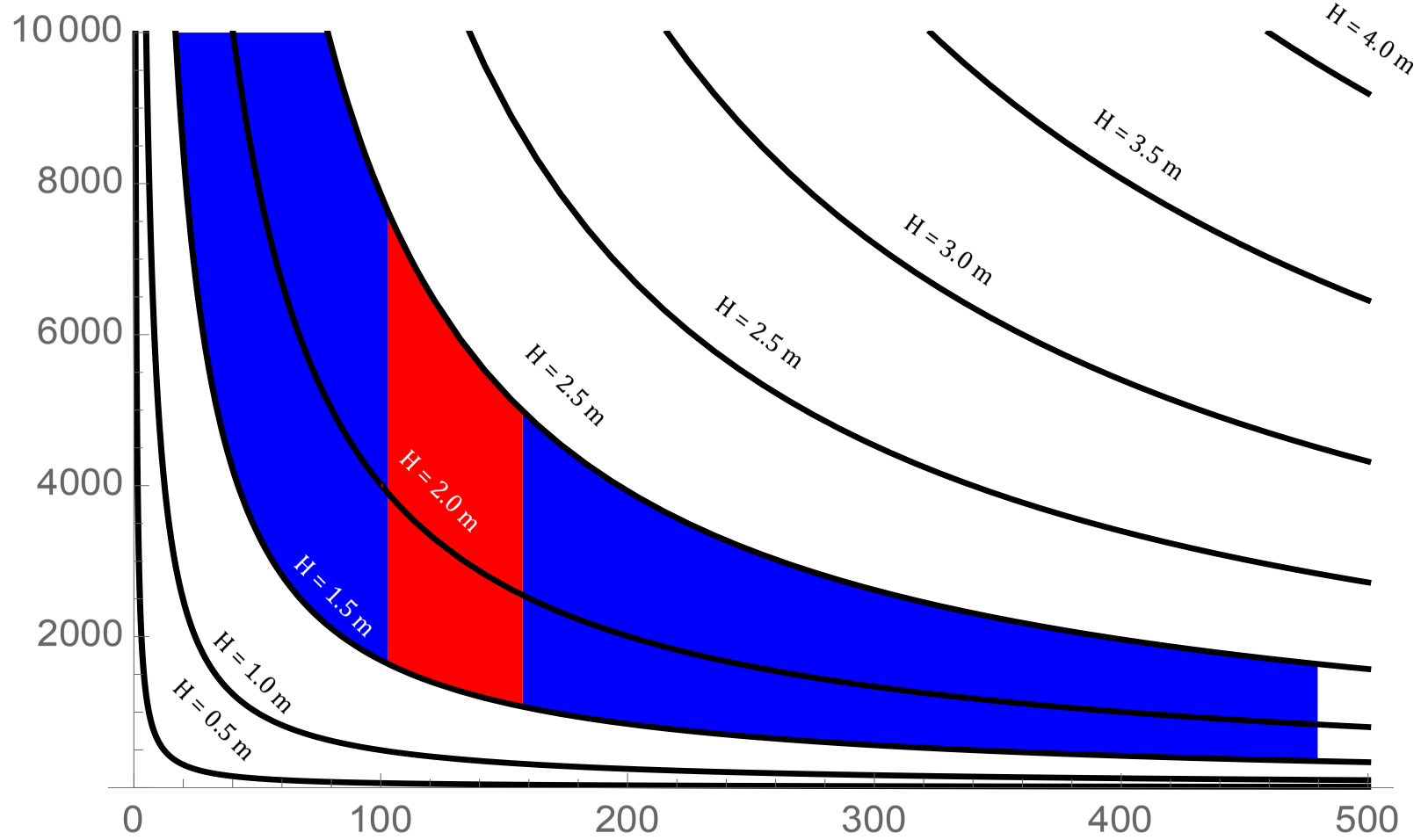

Figure 21 – Visual representation of the margin(s) of error associated with flow thickness (1.5-2.5 m) and viscosity [Pa s], and their effects on ranges of possible effusion rate values. The red zone represents the margin of error for viscosity solely based on the ±22% stemming from geochemical error (±3% SiO_2). The blue zone represents the much larger margin of error associated with uncertainty in the flow temperature calculations (≥ ±99%). The latter extends, on the y-axis, to an effusion rate of approx. $1x10^5$ m^3 s^{-1}. Model runs done according to Tallarico et al. (2006).

	visc_-20.56% = 102.33 Pa s	**visc_+23.03% = 158.49 Pa s**
thickness_-25% = 1.5 m	1731.7 $m^3 s^{-1}$	1118.1 $m^3 s^{-1}$
thickness_+25% = 2.5 m	8057.8 $m^3 s^{-1}$	5202.6 $m^3 s^{-1}$

Table 12 – Effusion rates calculated (using Tallarico et al., 2006) over the minimum and maximum viscosity and flow thickness values according to the margins of error calculated for those variables above.

	visc_-96.7% = 8.13 Pa s	**visc_+96.7% = 478.63 Pa s**
thickness_-25% = 1.5 m	21796.7 m^3 s^{-1}	370.238 m^3 s^{-1}
thickness_+25% = 2.5 m	101421 m^3 s^{-1}	1722.74 m^3 s^{-1}

Table 13 – Effusion rates calculated (using Tallarico et al., 2006) over the minimum and maximum viscosity and flow thickness values according to the margins of error calculated for those variables above, with viscosity accounting for temperature error.

Research Analysis

As a study in the feasibility of obtaining precise values for certain quantitative variables for very old and weathered flows, this research has significant value. By going through numerous quantitative and qualitative methods and connecting them to each other, analyzing each for potential influence on the overthickened morphologies of these lava flow units, I was able to determine which variables were most and least relevant and which were and were not feasibly quantifiable given the restrictions inherent in measuring such poorly-exposed units.

The first variable analyzed was geochemistry, and it was initially hypothesized that composition, weight percent SiO_2, in particular, would be a common thread among the three observed overthickened lava flow units. This was hypothesized for the sole reason that the only one of the three units that had previously undergone geochemical analysis, SB-N, also happened to be the only known flow on Banks Peninsula with a nephelinitic composition: thus, it seemed likely that the other two flows with similarly unique morphologies might share its geochemistry. This hypothesis was quickly disproven when the Northwest Bay unit was found to be a hawaiite and the East Okains Bay unit a mugearite. This is one area in which little uncertainty exists given the relative precision (±3%) of measurements made via XRF. Thus, geochemistry cannot be proven to be a significant control on the overthickened morphologies of these flows.

The next step in this process was to analyze the flows' viscosities using a quantitative model provided by Giordano et al. (2008). Since this variable is so heavily dependent upon a flow's silica content, conclusions on the role of viscosity in

these flows' emplacements reflected those drawn from their geochemistries. However, significantly more uncertainty exists when calculating viscosity. This is partially due to the lack of feasible means by which we can quantify the exact volatile contents of the old flows, but is mostly a product of our inability to accurately quantify flow temperatures. Along with geochemistry, temperature is the second primary independent variable in Giordano et al.'s (2008) viscosity model – and, while the former can be precisely quantified, temperatures are a much more complicated prospect.

Part of this ties back to the lack of methods by which we could determine precise volatile contents. For example, the viscosity of a lava flow with a given $\%SiO_2$ at 1100 ˚C with 0.1% H_2O will be much higher than the viscosity of a flow with the same $\%SiO_2$ and temperature with 5% H_2O. The literature on lava flow temperatures offers a vague range of possible temperatures for a lava type, and the geothermobarometry program MELTS was able to narrow this range by a bit. However, a large margin of error still exists. MELTS itself, built with the intention of being used for studying fractionation of subsurface magmas, was much less precise with regard to subaerial, low-pressure lava flows. As a result, a margin of error for temperature of approximately ±100 ˚C exists, which translates to a large margin of error for the viscosities derived from these temperatures, given the logarithmic relationship between flow temperature and flow viscosity.

The large uncertainties in viscosity that appear as a result of limitations in determining precise flow temperatures at the time of their emplacements, however, do not actually present a major problem in this part of our study. While they do

make it very difficult to obtain reasonably precise viscosity values, the close relationship of viscosity to geochemistry, for which there are precise values, means that conclusions drawn with respect to the role of geochemistry in these flows' emplacements and morphologies can be loosely applied to viscosity. Thus, while the margins of error associated with viscosity and temperature calculations make them very nearly completely unworkable, it still seems somewhat safe to conclude that viscosity did not play a common role in the development of the overthickened morphologies of NWB-H and SB-N.

With viscosity and geochemistry more-or-less ruled out as significant controls on these overthickened flow morphologies, the study next turned to effusion rates, which should play a major role in determining the final thickness of a lava flow. Among the methodologies used in this study, the Tallarico et al. (2006) model for effusion rates was unique in the sheer number of variables it involved. Thus, it was just as capable of precision as it was prone to errors, the latter a result of the pooling together of all previous variables, and their associated uncertainties, into the final product. The most significant of these errors and uncertainties are outlined in the previous chapter.

These sometimes large margins of error often associated with the effusion rate calculations stemming from the already significant error in flow temperature estimates travelling up the chain to viscosity and then to the effusion rate modeling prevent this study from determining a precise range of effusion rates. This, in turn, precludes us from drawing many strong conclusions with regard to the extent of the role of effusion rates in forming the flows' overthickened morphologies. As

mentioned in Chapter 8, one relatively strong conclusion that can be drawn is that these morphologies cannot have been *solely* a product of effusion rate. Again, this is due to the incredibly high effusion rate values calculated by the model when a flow thickness approaching the height of the largest sea cliffs (~40-50 m) is used in the model (Tallarico et al., 2006).

However, this specific case aside, it is difficult even to pinpoint a somewhat broad range of possible effusion rate values for the flow units. Again, we can refer to **Figure 21**, which highlights the range of possible effusion rate values given approximations of the margins of error we have associated with flow thickness and with viscosity (the latter an amalgamation of the margins of error for both $\%SiO_2$ and flow temperatures). When only considering the uncertainties in viscosity due to our geochemical measurements (the red area in **Figure 21**), we are left with a range of effusion rate estimates that, while not precise, does provide a somewhat reasonable idea of plausible values for this parameter. However, including the flow temperature uncertainties in the calculations (represented by the blue zone in **Figure 21**) yields a range of possible estimates for effusion rates that skyrockets to a minimum of ~370 $m^3 s^{-1}$ and a maximum of over $1.01x10^5$ $m^3 s^{-1}$, which translated to a margin of error >greater than ±99% (see **Table 13**). This effectively renders any attempts at precise estimates of effusion rates nearly useless.

Of the conclusions we have drawn here, most are negative: that is, they prove that something isn't the case rather than affirming a hypothesis or revealing new information. We can state, with relative certainty, that the overthickened morphologies of these lava flow units are not controlled to any significant degree by

geochemistry or, consequently, by the flows' viscosities during emplacement. A simple calculation using the Tallarico et al. (2006) model, while not entirely negating the influence of effusion rates on the flows' morphologies, does conclusively prove that the existence of the most abnormally thick parts of units SB-N and NWB-H cannot have solely been a product of high effusion rates. They might have played some role in these morphologies. In fact, it seems likely that they did, since even the lowest of calculated effusion rates for these flows are still somewhat high compared to "normal" basaltic effusion rates, but it is impossible to prove this either way here.

The only major variable left to assess is the role of paleo-topography in influencing the flows' morphologies during emplacement. This variable was not strictly quantifiable within the scope of this study, but it can be assessed qualitatively. In fact, given the uniquely variable dimensions of these flows – especially with regard to flow thicknesses – it seems very likely that, all other variables having been discounted or rendered inconclusive, topography was something that significantly influenced the morphology of flow units SB-N, NWB-H, and EOB-M.

The strongest evidence for this conclusion is displayed in **Figures 3 & 4**, both of which are found in Chapter 2. With Northwest Bay flow unit NWB-H standing out as a particularly clear example, note the somewhat rapid increase in flow thicknesses as the flows are traced toward the ocean. While the previously discussed uncertainties associated with the flows' widths and thicknesses (again, due to erosion and a frequent lack of clear exposures) might explain some of this

variability in thickness, it remains difficult to imagine that the systematic thickening of the flows from roughly 3 m to over 40 m could have merely been a product of erosion and vegetation cover. The most likely cause of this morphological pattern is that these units, during eruption and emplacement, flowed into a topographical depression and up against a wall. These ancient valleys would almost certainly have been erased over the past 6-10 million years, and would sufficiently explain why these flow units have such distinct morphologies among the rest of Banks Peninsula.

Future Work

Directions exist in which research could be expanded. Other flows with similar overthickened morphologies – both in Banks Peninsula and elsewhere – could be studied. There is also abundant room for further petrologic work on the Stony Bay nephelinite flow SB-N, expanding on the premise and conclusions of Eeg & Hampton (2014), as the reasons for its highly aberrant composition remain obscured. Its mantle source magma and its relationship to flows above and below it, in particular, are both topics that are ripe for further work. This study focused on the relationship (or lack thereof) of its odd geochemistry to its morphology, and only ever involved more in-depth geochemical analysis when it furthered that research aim. It remains the only known nephelinite unit in the entirety of Banks Peninsula, and a more detailed geochemical study – likely involving a much more thorough sampling approach that what thus study required – could shed light on its place within the greater Banks Peninsula geochemical sequence. This approach

might also utilize more extensive XRD analyses than were used for this particular study. Here, XRD analyses were only ever used to confirm the presence of minerals observed in thin section.

Aside from expanding the scope of this research, it would be advisable for any continuations of this or similar work involving these flows' morphologies to put focus on reducing the number and scope of the uncertainties and errors that have so obfuscated many of the conclusions drawn from this study. The most crucial of these uncertainties lies in the eruptive temperatures of the lava flows in question. Further work with MELTS or similar programs may or may not shed further light on the requisite flow temperatures, especially in conjunction with more detailed petrologic studies of these lavas. Constraining flow temperatures would significantly narrow our margins of error for viscosities and effusion rates, and should therefore be a priority in future studies.

Other sources of error, such as flow widths and flow thicknesses, could potentially have their effects reduced by allowing significantly more time for field surveys of the flows. Thus study was limited by both time and equipment, and a detailed survey of flow thickness in particular along the flow sections in question would significantly reduce error. More accurate GPS units, in particular, would be extremely helpful here. Large stretches of the flow units – namely the thickest sea cliff sections – were completely inaccessible with regard to either sampling or manual measurements. GPS units with greatly increased precision would allow further studies of these flows to obtain much more accurate thicknesses (and widths) by taking measurements at the tops and bottoms of the flows. In a similar

vein, given increased time, access to a boat would be helpful to survey the seaward sections of the flow units. This would especially help in the case of the comparatively inaccessible East Okains Bay mugearite flow unit EOB-M, which was barely touched upon in this study due to time and accessibility concerns.

Further time spent undertaking detailed dimensionally-focused field surveys would not only assist with reducing uncertainty in these calculations, but could also expand future studies into entirely new areas. While aerial imagery did not yield much in the way of total length of these flows due to vegetation cover, tracing the flows inland on foot could both provide further insight into the extent of the flows and potentially pinpoint a source vent for each flow. One particularly ambitious project might be to put focus entirely on the dimensions of one of these flows and create a three-dimensional model of the flow and the topography on which it was emplaced. This hypothetical model could be used to calculate a rough volume, which would then be combined with more precise effusion rate and viscosity estimates to yield the duration of the lava flow's emplacement.

After processes relating to the actual eruptions of the flows, such as viscosity and effusion rate, are better constrained, the next logical step in reconstructing the emplacement of the three overthickened flows is to model and quantify their cooling rates. This may be especially useful due to the unique nature of the overthickened sections, in which joints often propagate through flow boundaries, suggesting rapid emplacement of successive, thinner flows in a small enough timespan to form a single simple cooling unit. This would depend heavily upon measurements being taken of the columnar joints present at all three units, since these features are

intrinsically tied to a flow's thermal gradient and cooling rate, allowing for mathematical models to be constructed based on their dimensions (Budkewitsch & Robin, 1994; Grossenbacher & McDuffie, 1995). This would also be relevant to the role of potentially very high effusion rates in these flows' emplacement, since columnar joints in the thickest sections of the flows tend to propagate vertically across discrete flow boundaries. This may indicate rapid pulses of lava being emplaced on top of one another in quick enough succession to cool as a single temporal unit.

Chapter 10 – Conclusion

This study began as an attempt to relate the unique nephelinite composition of unit SB-N to its unique overthickened morphology and, subsequently, to the similar morphologies of units NWB-H and EOB-M. This was quickly disproven when the latter two flows were analyzed and shown to be, respectively, a hawaiite and a mugearite flow. This turned out to be only the first step in a long, multi-step process of trial and error in which I sought to determine the answer to the following question: if there is no apparent correlation between geochemistry and these flows' unique morphologies, then what other variables – if any – could be connected to the existence of the flows' sheer 40-60 m sea cliffs?

Candidates included several quantifiable rheological parameters, particularly viscosity and effusion rate, both of which should have a significant influence on the final morphology of a lava flow. Viscosity was analyzed using a model developed by Giordano et al. (2008), and was supplemented by a program called MELTS, developed by Ghiorso & Sack (1995), that was used in an attempt to narrow down the range of flow temperature estimates used in the viscosity calculations. The importance of $\%SiO_2$ and flow temperature in controlling a flow's viscosity was observed. Uncertainties related to flow temperatures prevented this model from yielding any truly precise ranges of viscosities for the overthickened flow units: however, given the close relationship between $\%SiO_2$ and viscosity, it was concluded that the latter likely had little to no influence on the overthickened morphology shared between the three flows.

Next, a model developed by Tallarico et al. (2006) was used to estimate the effusion rates that produced these flows, with particular focus on the NWB-H and SB-N units. Calculations generally yielded somewhat high effusion rates relative to known basaltic effusion rates, but, again, significant uncertainties prevented strong conclusions or precise ranges of values to be produced. The large margin of error left at the end of the viscosity calculations as a result of uncertainties in flow temperatures carried over to and was magnified even further in the effusion rate step, resulting in unreasonable ranges of values. It was definitively shown by this model that the thickest sections of these flows could not have been formed purely by high effusion rates, since the necessary values for that variable were orders of magnitude greater than has been observed on Earth.

Left with an abundance of disproven hypotheses and unworkable margins of error, this study became, in its end, a study of how feasible it is to attempt such precise quantifications of rheological parameters for ancient lava flows. Many of the models used in these calculations were developed via observations of modern, active flows, and when applied to lava flows as eroded, inaccessible, and poorly exposed as those on Banks Peninsula, there was often too much uncertainty to yield any precise conclusions. In fact, the most likely cause of the overthickened morphologies of these flows is likely to be, rather than any specific geochemical or rheological parameter, the ancient topography in and across which they were emplaced when erupted.

Future work in this area could involve attempts to cull the uncertainty associated with flow dimensions and flow temperatures. Work on flow dimensions,

in particular, could be used to quantify paleo-topography, which could then be used to calculate the duration of the eruptions. Tied to this are cooling rates, which might be estimated from observations of columnar joint dimensions. Further study in this area could serve to illuminate the mechanism by which the overthickened sections were emplaced (i.e. flow inflation vs. discrete pulses of lava successively emplaced on top of each other).

References Cited

Budkewitsch, P., and Robin, P.Y., 1994, Modeling the evolution of columnar joints: Journal of Volcanology and Geochemical Research, v. 59, no. 3, p. 219-239, doi: 10.1016/0377-0273(94)90092-2.

Bultitude, R.J., and Green, D.H., 1967, Experimental Study at High Pressures on the Origin of Olivine Nephelinite and Olivine Melilite Nephelinite Magmas: Earth and Planetary Science Letters, v. 3, p. 325–337.

Campbell, H., Malahoff, A., Browne, G., Graham, I., and Sutherland, R., 2012, New Zealand Geology: Episodes, v. 35, no. 1, p. 57-71.

Dragoni, M., Piombo. A., and Tallarico, A., 1995, A model for the formation of lava tubes by roofing over a channel: Journal of Geophysical Research, v. 100, no. B5, p. 8435-8447, doi: 10.1029/94JB03263

Eeg, H., and Hampton, S., 2014, Understanding an olivine-nephelinite lava flow : implications for the Akaroa Volcanic Complex: , p. 1–21.

Gee, L.L., and Sack, R.O., 1988, Experimental petrology of melilite nephelinites: Journal of Petrology, v. 29, no. 6, p. 1233–1255, doi: 10.1093/petrology/29.6.1233.

Ghiorso, M.S., and Sack, R.O., 1995, Chemical mass transfer in magmatic processes IV. A revised and internally consistent thermodynamic model for the interpolation and extrapolation of liquid-solid equilibria in magmatic systems at elevated temperatures and pressures: Contributions to Mineralogy and Petrology, v. 119, no. 2-3, p. 197–212, doi: 10.1007/BF00307281.

Giordano, D., Russell, J.K., and Dingwell, D.B., 2008, Viscosity of magmatic liquids: A model: Earth and Planetary Science Letters, v. 271, no. 1-4, p. 123–134, doi: 10.1016/j.epsl.2008.03.038.

Grossenbacher, K.A., and McDuffie, S.M., 1995, Conductive cooling of lava: Columnar joint diameter and stria width as functions of cooling rate and thermal gradient: Journal of Volcanology and Geothermal Research, v. 69, no. 1-2, p. 95-103, doi: 10.1016/0377-0273(95)00032-1.

Gualda, G.A.R., and Ghiorso, M.S., 2015, MELTS_Excel: A Microsoft Excel-based MELTS interface for research and teaching of magma properties and

evolbution: Geochemistry,Geophysics,Geosystems, v. 16, p. 315–324, doi: 10.1002/2014GC005545.Received.

Hampton, S.J., and Cole, J.W., 2009, Lyttelton Volcano, Banks Peninsula, New Zealand: Primary volcanic landforms and eruptive centre identification: Geomorphology, v. 104, no. 3-4, p. 284–298, doi: 10.1016/j.geomorph.2008.09.005.

Harris, A.J.L., and Rowland, S.K., 2009, Effusion rate controls on lava flow length and the role of heat loss: A review: Special Publications of IAVCEI, v. 2, p. 33–51.

Harris, A.J.L., and Rowland, S.K., 2001, FLOWGO: A kinematic thermo-rheological model for lava flowing in a channel: Bulletin of Volcanology, v. 63, no. 1, p. 20–44, doi: 10.1007/s004450000120.

Hulme, G., 1974, The interpretation of lava flow morphology: Geophysical Journal International, v. 39, p. 361-383, doi: 10.1111/j.1365-246X. 1974.tb05460.

Kilburn, C.R.J., 2000, Lava flows and flow fields: Encyclopedia of Volcanoes, 291-305

Patrick, M.R., Dehn, J., and Dean, K., 2004, Numerical modeling of lava flow cooling applied to the 1997 Okmok eruption: Approach and analysis: Journal of Geophysical Research, v. 109, no. B3, p. 1–17, doi: 10.1029/2003JB002537.

Pearce, J.A., and Cann, J.R., 1973, Tectonic setting of basic volcanic rocks determined using trace element analyses: Earth and Planetary Science Letters, v. 19, p. 290-300, doi: 10.1016/0012-821X(73)90129-5.

Pearce, J.A., and Norry, M.J., 1979, Petrogenetic implications of Ti, Zr, Y, and Nb variations in volcanic rocks: Contributions to Mineralogy and Petrology, v. 69, no. 1, p. 33-47, doi: 10.1007/BF00375192

Platz, T., Foley, S.F., and André, L., 2004, Low-pressure fractionation of the Nyiragongo volcanic rocks, Virunga Province, D.R. Congo: Journal of Volcanology and Geothermal Research, v. 136, p. 269–295, doi: 10.1016/j.jvolgeores.2004.05.020.

Price, R.C., and Taylor, S.R., 1980, Petrology and geochemistry of the Banks Peninsula volcanoes, South Island, New Zealand: Contributions to Mineralogy and Petrology, v. 72, no. 1, p. 1–18, doi: 10.1007/BF00375564.

Sawyer, G.M., Carn, S.A., Tsanev, V.I., Oppenheimer, C., and Burton, M., 2008, Investigation into magma degassing at Nyiragongo volcano, Democratic Republic of the Congo: Geochemistry, Geophysics, Geosystems, v. 9, December 2007, p. 1-17, doi: 10.1029/2007GC001829

Sewell, R.J., 1988, Late Miocene Volcanic Stratigraphy of Central Banks Peninsula, Canterbury, New Zealand: New Zealand Journal of Geology and Geophysics, v. 31, no. March 2015, p. 41–64, doi: 10.1080/00288306.1988.10417809.

Stipp, J.J., and McDougall, I., 1968, Geochronology of the Banks Peninsula Volcanoes, New Zealand: New Zealand Journal of Geology and Geophysics, v. 11, no. 5, p. 1239–1258, doi: 10.1080/00288306.1968.10420260.

Tallarico, A., Dragoni, M., and Zito, G., 2006, Evaluation of lava effusion rate and viscosity from other flow parameters: Journal of Geophysical Research: Solid Earth, v. 111, no. 11, p. 1–7, doi: 10.1029/2005JB003762.

Thordarson, T., and Self, S., 1993, The Laki (Skaftár Fires) and Grímsvötn eruptions in 1783-1785: Bulletin of Volcanology, v. 55, p. 233–263.

Timm, C., Hoernle, K., van den Bogaard, P., Bindeman, I., and Weaver, S., 2009, Geochemical evolution of intraplate volcanism at Banks Peninsula, New Zealand: Interaction between asthenospheric and lithospheric melts: Journal of Petrology, v. 50, no. 6, p. 989–1023, doi: 10.1093/petrology/egp029.

Appendix A: Expanded Tables of Effusion Rate Results

	μ = 25 Pa s	μ = 50 Pa s	μ = 75 Pa s	μ = 100 Pa s	μ = 150 Pa s
H = 0.5 m	341.188	170.594	113.729	85.297	56.8647
H = 1.0 m	2782.60	1391.30	927.535	695.651	463.767
H = 1.5 m	9451.04	4725.52	3150.35	2362.76	1575.17
H = 2.0 m	22473.3	11236.6	7491.1	5618.32	3745.55
H = 2.5 m	43976.2	21988.1	14658.7	10994	7329.36
H = 3.0 m	76086.4	38043.2	25362.1	19021.6	12681.1
H = 3.5 M	120931	60465.4	40310.3	30232.7	20155.1
H = 4.0 m	180636	90318.1	60212.1	45159.1	30106
H = 4.5 m	257329	128665	85776.5	64332.4	42888.2
H = 5.0 m	353137	176569	117712	88284.3	58856.2
H = 40 m	1.8140E+08	9.0701E+07	6.0467E+07	4.5350E+07	3.0234E+07

	μ = 200 Pa s	μ = 250 Pa s	μ = 300 Pa s	μ = 350 Pa s	μ = 400 Pa s
H = 0.5 m	42.6485	34.1188	28.4323	24.3706	21.3243
H = 1.0 m	347.826	278.26	231.884	198.757	173.913
H = 1.5 m	1181.38	945.104	787.587	675.075	590.69
H = 2.0 m	2809.16	2247.33	1872.77	1605.24	1404.58
H = 2.5 m	5497.02	4397.62	3664.68	3141.15	2748.51
H = 3.0 m	9510.8	7608.64	6340.53	5434.74	4755.4
H = 3.5 M	15116.4	12093.1	10077.6	8637.92	7558.18
H = 4.0 m	22579.5	18063.6	15053	12902.6	11289.8
H = 4.5 m	32166.2	25732.9	21444.1	18380.7	16083.1
H = 5.0 m	44142.2	35313.7	29428.1	25224.1	22071.1
H = 40 m	2.2675E+07	1.8140E+07	1.5117E+07	1.2957E+07	1.1338E+07

	μ = 450 Pa s	μ = 500 Pa s	μ = 550 Pa s	μ = 600 Pa s	μ = 650 Pa s
H = 0.5 m	18.9549	17.0594	15.5085	14.2162	13.1226
H = 1.0 m	154.589	139.13	126.482	115.942	107.023
H = 1.5 m	525.058	472.552	429.593	393.794	363.502
H = 2.0 m	1248.52	1123.66	1021.51	936.387	864.358
H = 2.5 m	2443.12	2198.81	1998.92	1832.34	1691.39
H = 3.0 m	4227.02	3804.32	3458.47	3170.27	2926.4
H = 3.5 M	6718.38	6046.54	5496.86	5038.79	4651.19
H = 4.0 m	10035.3	9031.81	8210.74	7526.51	6947.55
H = 4.5 m	14296.1	12866.5	11696.8	10722.1	9897.29
H = 5.0 m	19618.7	17656.9	16051.7	14714.1	13582.2
H = 40 m	1.0078E+07	9.0701E+06	8.2455E+06	7.5584E+06	6.9770E+06

	μ = 700 Pa s	μ = 750 Pa s	μ = 800 Pa s	μ = 850 Pa s	μ = 900 Pa s
H = 0.5 m	12.1853	11.3729	10.6621	10.0349	9.47745
H = 1.0 m	99.3787	92.7535	86.9564	81.8413	77.2946
H = 1.5 m	337.537	315.035	295.345	277.972	262.529
H = 2.0 m	802.618	749.11	702.291	660.979	624.258
H = 2.5 m	1570.58	1465.87	1374.25	1293.42	1221.56
H = 3.0 m	2717.37	2536.21	2377.7	2237.84	2113.51
H = 3.5 M	4318.96	4031.03	3779.09	3556.79	3359.19
H = 4.0 m	6451.3	6021.21	5644.88	5312.83	5017.67
H = 4.5 m	9190.34	8577.65	8041.55	7568.51	7148.04
H = 5.0 m	12612	11771.2	11035.5	10386.4	9809.37
H = 40 m	6.4786E+06	6.0467E+06	5.6688E+06	5.3353E+06	5.0389E+06

	μ = 950 Pa s	μ = 1000 Pa s
H = 0.5 m	8.97863	8.5297
H = 1.0 m	73.2264	69.5651
H = 1.5 m	248.712	236.276
H = 2.0 m	591.403	561.832
H = 2.5 m	1157.27	1099.4
H = 3.0 m	2002.27	1902.16
H = 3.5 M	3182.39	3023.27
H = 4.0 m	4753.59	4515.91
H = 4.5 m	6771.83	6433.24
H = 5.0 m	9293.08	8828.43
H = 40 m	4.7737E+06	4.5350E+06

Appendix B: Complete Geochemical Data

Major oxides: Colorado College XRF

Compound	NWB1a	NWB2	BPSB1	BPSB2	BPSB3	BPSB4	BPSB5
$\%SiO_2$	46.702	45.761	n/a	40.639	40.251	39.340	39.979
$\%Na_2O$	1.859	1.839	n/a	1.859	1.859	1.992	1.859
%MgO	7.583	9.112	n/a	11.747	11.927	12.232	11.627
$\%Al_2O_3$	14.945	14.504	n/a	11.636	11.478	11.004	11.349
$\%P_2O_5$	0.391	0.271	n/a	0.981	0.973	0.989	1.005
$\%K_2O$	0.839	0.716	n/a	1.090	1.224	1.586	1.220
%CaO	10.468	11.112	n/a	11.593	11.775	11.590	11.871
$\%TiO_2$	3.194	3.192	n/a	3.632	3.689	3.404	3.457
%MnO	0.168	0.164	n/a	0.200	0.202	0.204	0.204
$\%FeO_2$	13.789	13.328	n/a	15.154	15.378	15.364	15.445

Compound	BPSB6	BPSB7	BPSB8	BPSB9	BPSB10	BPSB11	BPSB12
$\%SiO_2$	47.925	41.490	47.808	47.284	40.125	49.031	47.542
$\%Na_2O$	2.664	1.859	1.859	1.859	1.859	3.320	1.859
%MgO	3.838	10.721	4.228	5.410	11.331	3.127	4.901
$\%Al_2O_3$	16.999	12.294	16.802	16.283	11.701	16.514	16.490
$\%P_2O_5$	0.593	0.947	0.544	0.529	1.005	1.029	0.577
$\%K_2O$	1.377	0.898	1.360	1.362	1.373	1.924	1.423
%CaO	8.209	11.816	8.467	8.640	11.722	6.647	8.325
$\%TiO_2$	3.455	3.268	3.354	3.338	3.649	2.157	3.292
%MnO	0.148	0.196	0.166	0.179	0.206	0.228	0.172
$\%FeO_2$	13.800	15.101	13.490	13.468	15.311	12.820	13.450

Trace & REEs: Colorado College XRF

Element	NWB1a	NWB2	BPSB1	BPSB2	BPSB3	BPSB4	BPSB5
Sc [ppm]	47.1	46.7	46.2	49.7	49.1	45.8	44.9
V [ppm]	282.9	225.4	114.9	245.6	252.9	208.4	216.5
Cr [ppm]	210.4	196.0	181.2	155.8	198.4	162.4	140.3
Co [ppm]	33.0	36.3	27.8	35.7	44.7	34.7	33.9
Ni [ppm]	127.2	112.3	104.7	136.4	161.2	143.5	132.4
Cu [ppm]	82.8	78.7	38.0	38.0	52.0	43.5	42.6
Rb [ppm]	17.9	16.0	22.8	38.5	27.1	31.2	24.7
Sr [ppm]	597.4	609.8	732.3	1073.7	1060.0	1216.3	1189.8
Y [ppm]	23.0	30.6	21.6	28.1	26.6	28.7	29.2
Zr [ppm]	176.5	144.6	237.8	316.8	313.4	343.0	334.3
Nb [ppm]	40.0	31.2	60.1	84.8	81.2	88.0	84.5
La [ppm]	28.1	27.0	40.4	48.5	52.1	57.9	58.1
Ce [ppm]	48.8	39.8	88.6	109.3	109.6	119.3	117.7
Pr [ppm]	5.3	4.4	10.4	13.1	12.6	13.9	13.9
Nd [ppm]	24.5	25.4	50.5	61.0	58.3	61.6	60.7
Sm [ppm]	5.7	6.9	10.7	11.5	8.6	11.0	12.2
Gd [ppm]	6.4	5.3	10.8	9.6	7.3	8.7	10.0
Dy [ppm]	3.2	5.3	4.1	7.1	6.3	6.9	6.5
Yb [ppm]	1.2	2.7	1.0	3.7	3.5	3.6	3.0
Zn [ppm]	90.0	73.5	72.2	117.1	123.4	116.0	105.4
Ga [ppm]	16.8	16.2	17.2	19.5	19.2	21.6	18.3
Ba [ppm]	261.4	215.0	332.3	410.9	374.3	438.4	445.3
Th [ppm]	-1.3	-1.3	3.4	-1.3	-1.3	2.6	2.9
U [ppm]	1.9	1.9	1.9	1.9	1.9	1.9	1.9
Na [%]	3.1	3.1	3.1	3.1	3.1	3.1	3.1
Sum [%]	3.3	3.3	3.4	3.4	3.4	3.5	3.4

Trace & REEs: Colorado College XRF (cont'd)

Element	BPSB6	BPSB7	BPSB8	BPSB9	BPSB10	BPSB11	BPSB12
Sc [ppm]	38.4	50.4	40.7	39.2	48.9	28.0	38.6
V [ppm]	244.3	268.4	205.5	184.0	261.0	52.9	184.8
Cr [ppm]	-4.7	203.3	1.1	3.6	209.8	33.8	2.4
Co [ppm]	34.8	40.2	24.9	29.0	37.1	25.2	29.6
Ni [ppm]	14.0	184.9	34.2	14.0	151.1	14.0	14.0
Cu [ppm]	23.9	54.6	27.9	28.3	52.0	6.3	24.1
Rb [ppm]	36.3	8.8	32.2	30.4	36.1	40.9	33.7
Sr [ppm]	693.9	946.3	700.8	918.8	1123.8	745.8	672.8
Y [ppm]	31.4	27.5	29.6	25.6	28.9	43.0	30.8
Zr [ppm]	240.0	261.9	233.2	225.5	327.6	347.3	239.3
Nb [ppm]	51.5	75.8	49.5	46.5	85.6	86.3	51.5
La [ppm]	39.8	50.4	36.8	31.4	51.5	56.1	36.6
Ce [ppm]	72.0	97.8	64.2	64.8	111.0	110.7	68.1
Pr [ppm]	7.9	11.1	7.1	7.1	12.9	12.8	7.9
Nd [ppm]	35.8	50.2	38.7	32.6	64.2	57.0	35.2
Sm [ppm]	7.3	7.3	7.1	5.4	9.7	9.6	7.3
Gd [ppm]	6.8	6.6	6.6	5.0	9.7	8.1	9.5
Dy [ppm]	5.0	5.0	6.3	5.0	6.8	8.4	4.6
Yb [ppm]	2.4	2.6	3.7	2.8	3.8	5.2	2.2
Zn [ppm]	127.5	113.8	104.8	89.5	127.2	127.5	100.0
Ga [ppm]	22.2	16.4	20.2	18.0	18.9	24.9	20.8
Ba [ppm]	716.0	487.5	836.9	320.9	414.2	485.1	344.3
Th [ppm]	2.7	2.3	2.3	-1.3	2.4	3.1	2.7
U [ppm]	1.9	1.9	1.9	1.9	1.9	1.9	1.9
Na [%]	3.1	3.1	3.1	3.1	3.1	3.1	3.9
Sum [%]	3.4	3.4	3.4	3.3	3.5	3.4	4.1

Major oxides: University of Canterbury XRF

Compound	SB7	SB-AB	SB-AB2	SB-AG	NWB-14	EO-1
$\%SiO_2$	40.31	40.98	40.11	40.10	47.40	51.95
$\%Na_2O$	4.59	4.74	4.80	4.32	4.70	5.98
%MgO	11.08	11.22	11.41	10.97	4.10	2.23
$\%Al_2O_3$	12.25	12.25	12.36	12.26	17.03	17.71
$\%P_2O_5$	0.93	0.82	0.84	0.94	0.89	0.77
$\%K_2O$	1.15	1.15	1.11	1.26	1.60	2.88
%CaO	11.28	10.91	11.13	11.39	7.80	5.33
$\%TiO_2$	3.55	3.53	3.59	3.70	3.06	1.59
%MnO	0.20	0.197	0.199	0.200	0.21	0.23
$\%FeO_2$	14.66	14.20	14.46	14.87	13.22	11.33